

Euclid

Galaxy SED reconstruction in the PHZ processing function: impact on the PSF and the role of medium-band filters

Euclid Collaboration: F. Tarsitano, C. Schreiber, H. Miyatake, A. J. Nishizawa, W. G. Hartley, L. Miller, C. Cragg, B. Csizi, H. Hildebrandt et al.

(Full author list and affiliations details can be found after the references)

January 19, 2026

ABSTRACT

Weak lensing surveys require accurate correction for the point spread function (PSF) when measuring galaxy shapes. For a diffraction-limited PSF, as arises in space-based missions, this correction depends on each galaxy's spectral energy distribution (SED), hence a sufficiently accurate knowledge of the SED is needed for every galaxy. In the *Euclid* mission, galaxy SED reconstruction, which is one of the tasks of the photometric-redshift processing function (PHZ PF), relies on broad- and medium-band ancillary photometry. The limited wavelength sampling of the I_E passband and signal-to-noise ratio may affect the reconstruction accuracy and translate into biases in the weak lensing measurements. In this study, we present the methodology, which is employed in the *Euclid* PHZ PF, for reconstructing galaxy SEDs at 55 wavelengths, sampling the I_E passband every 10 nm, and we assess whether it fulfils the accuracy requirements imposed on the *Euclid* PSF model. We employ both physics- and data-driven methods, focusing on a new approach of template-based flux correction and Gaussian processes. For validation, we introduce an SED metric whose bias translates into inaccuracies in the PSF quadrupole moments. Our findings demonstrate that Gaussian processes and template fitting meet the requirements only in specific, but complementary, redshift intervals. We therefore propose a hybrid approach, which leverages both methods. This solution proves to be effective in meeting the *Euclid* accuracy requirements for most of the redshift range of the survey. Finally, we investigate the impact on the SED reconstruction of a new set of 16 evenly-spaced medium-band filters for the Subaru telescope, providing quasi-spectroscopic coverage of the I_E passband. This study shows promising results, ensuring accurate SED reconstruction and meeting the mission PSF requirements. This work thus provides not only the methodological foundation of galaxy SED reconstruction in the *Euclid* PHZ PF, but also a roadmap for future improvements using a new medium-band survey.

Key words. Galaxies: evolution, photometry; Cosmology; Methods: statistical, numerical.

1. Introduction

Our understanding of the Universe has been significantly changed by [Riess et al. \(1998\)](#) and [Perlmutter et al. \(1999\)](#), who provided observational evidence of an accelerated cosmic expansion. Since then, this discovery has been confirmed by a wide range of observations, yet the underlying theory is still debated, as competing explanations range from a change of the fundamental physics to generalisations of the FLRW cosmologies (e.g., [Copeland et al. 2006](#); [Bamba et al. 2012](#); [Clifton et al. 2012](#); [Nojiri et al. 2017](#); [Heisenberg et al. 2018, 2023](#)). Among the cosmological models proposed so far, the most relevant is Λ CDM, based on two elements, a positive cosmological constant ($\Lambda > 0$) and the cold dark matter (CDM) paradigm ([Abdalla et al. 2022](#)). Λ CDM provides a simple yet powerful description of the Universe, based on parameters including the Hubble constant, which sets the expansion rate of the Universe; the relative densities of dark energy, dark matter and ordinary matter; the curvature of the Universe and other quantities describing the cosmic microwave background (CMB). Driven by advances in observational and computational capabilities, cosmologists have been making remarkable progress in constraining these parameters, with uncertainties of just a few percent, a precision that was unimaginable just three decades ago ([Turner 2022](#)). However, despite such advances, Λ CDM still lacks an adequate explanation for dark mat-

ter and dark energy ([Frieman et al. 2008](#); [Weinberg et al. 2013](#); [Perivolaropoulos & Skara 2022](#); [Efstathiou 2025](#)). Advancing our current knowledge requires detailed measurements of both the expansion history of the Universe and the growth of structures as a function of cosmic time. This will be possible through Stage IV surveys such as *Euclid*, a mission of the European Space Agency (ESA) whose core science is devoted to the investigation of the Dark Universe.

The Euclid Wide Survey (EWS; [Laureijs et al. 2011](#); [Racca et al. 2016](#); [Euclid Collaboration: Scaramella et al. 2022](#); [Euclid Collaboration: Mellier et al. 2025](#)) is set to cover 14 000 deg² of the extragalactic sky in six years. It uses two instruments, VIS ([Euclid Collaboration: Cropper et al. 2025](#)) and the Near-Infrared Spectrometer and Photometer (NISP; [Euclid Collaboration: Jahnke et al. 2025](#)). The VIS instrument is a broadband optical imager specifically designed for imaging galaxies in the wavelength range 550–900 nm, with a spatial resolution of 0''.18. NISP serves as an imager in the near-infrared (NIR) bands Y_E , J_E , H_E , combining capabilities with a NIR slitless spectrograph ([Euclid Collaboration: Schirmer et al. 2022](#)).

Euclid science focuses on two principal probes: galaxy clustering at $z > 0.9$ through NIR slitless spectroscopy, and the matter distribution as a function of redshift using photometric galaxy clustering and weak gravitational lensing. The latter causes distortions of the images of distant galaxies whose light gets deflected by intervening large-

scale structures. Due to this phenomenon, slight distortions in the apparent shape of galaxies are observed, with adjacent galaxies exhibiting alignment patterns across the sky. Comprehensive reviews on the weak-lensing techniques were provided by [Bartelmann & Schneider \(2001\)](#), [Hoekstra & Jain \(2008\)](#), [Kilbinger \(2015\)](#) and [Bartelmann & Maturi \(2017\)](#). Early studies were presented in [Wittman et al. \(2000\)](#), using galaxy images observed with the Big Throughput Camera ([Wittman et al. 1998](#)), in [Bacon et al. \(2000\)](#) using data from the William Herschel Telescope ([Bacon 2001](#)), and by [Kaiser et al. \(2000\)](#) and [Van Waerbeke et al. \(2001\)](#), providing shear measurements for the Canada France Hawaii Telescope survey ([Monet & et al. 1998](#)). An analysis of CFHTLenS by [Heymans et al. \(2012, 2013\)](#) was followed up with the first measurements from the Kilo-Degree Survey (KiDS; [de Jong et al. 2013](#); [Hildebrandt et al. 2017](#)). More recent works probed the cosmological model through cosmic shear measurements using the Dark Energy Survey ([Troxel et al. 2018](#); [Amon et al. 2022](#); [Secco et al. 2022](#); [Abbott et al. 2023](#)) and KiDS ([Asgari et al. 2021](#); [Wright et al. 2025](#); [Stölzner et al. 2025](#)).

The major challenge in measuring the cosmic shear signal is that the typical change in a galaxy shape is tiny compared to other effects such as projection and statistical noise ([Kilbinger 2015](#)). To cope with these relatively large statistical uncertainties, cosmic shear estimates are obtained by averaging over a large number of galaxies. During its observational campaign, *Euclid* will provide shape measurements for billions of galaxies, allowing a significant decrease in statistical uncertainties through the averaging of individual measurements. However, for the results to be meaningful, and to fully exploit the potential of the *Euclid* survey, a consistent reduction in the level of residual systematics is required. Instrumental effects altering galaxy shapes can overwhelm the lensing signal, and the most significant of them is the point spread function (PSF; [Massey et al. 2007](#); [Mandelbaum et al. 2005](#)).

In an effort to understand how PSF systematic errors affect weak lensing analyses, a series of studies presented analytical models propagating those errors through weak lensing measurements. [Paulin-Henriksson et al. \(2008\)](#) and [Massey et al. \(2013\)](#), hereafter M13, introduced an analytical framework assessing the multiplicative and additive biases in weak lensing shear that arise from errors in the assumed PSF model. Those authors showed that we expect multiplicative bias to be produced by errors in the assumed PSF size, and additive biases to be driven by errors in PSF size or ellipticity. The studies presented in M13 laid the foundation for a detailed propagation of systematic effects presented by [Cropper et al. \(2013\)](#), hereafter C13, where they focus on defining the characteristics and the requirements of space-based weak lensing experiments, and proposing error budgets for the various effects that enter a weak lensing analysis. This work, in turn, has been taken as a reference for the *Euclid* mission.

Diffraction-limited telescopes, such as the *Euclid* payload, have chromatic PSFs that depend on the SED of the star or galaxy being observed, due to the Fraunhofer diffraction pattern of the entrance pupil. Each wavelength in the *Euclid* I_E bandpass makes a contribution to the integrated broadband PSF, where the monochromatic PSF contributions have sizes that increases with wavelength, but with more complex profile changes also present, arising from the mixture of optical wavefront error (which itself is chromatic), chromatic detector PSF contributions and achromatic guiding error. The effects of chromatic PSF models, in the context of the *Euclid* mission, were studied by [Cypriano et al. \(2010\)](#), hereafter C10, and [Semboloni et al. \(2013\)](#). The latter focused on the bias introduced through the

spatial variation of the galaxy colour. C10 explored a method to predict the PSF size as a function of galaxy colours, using stars with colours closer to the galaxies. An analogous work was conducted by [Meyers & Burchat \(2015\)](#) for ground-based data. [Eriksen & Hoekstra \(2018\)](#), hereafter EH18, revisited the method proposed in C10, studying the bias in the wavelength-dependent *Euclid* PSF model caused by the limited broad-band-based information about the galaxy SEDs. Their findings suggested that the requirements indicated in M13 and C13 can be achieved using the photometric dataset used for *Euclid* photometric redshift estimates.

Galaxy SEDs can be determined either through spectroscopy or photometry. In the first case, the emitted light is dispersed into its constituent wavelengths, allowing the measurement of the corresponding fluxes and the identification of spectral features such as emission and absorption lines. In the second case, the flux is measured through different filters, which can be narrow (typically in the range $[10, 20]$ Å), medium (spanning the range $[100, 200]$ Å) or broad (in the interval $[500, 1000]$ Å). Multiple photometric observations are taken across a range of wavelengths, and the resulting data points are used to construct the SED. In a basic approach, the SED is given by interpolation methods (e.g., linear, cubic spline) of the flux points. Advanced regression methods are also available, such as the machine learning algorithm Gaussian processes (GP), which provide a functional form of the SED through a cross-correlation between flux points. While these methods can be used to reconstruct the galaxy SEDs solely relying on data, another approach is to make use of prior knowledge about the SED shapes. Known as template fitting (TF), this method compares the photometric sample to a set of predefined templates that represent different types of galaxies. Biases in this technique arise from potential template mismatches.

In comparison, spectroscopy appears to be ideally suited to the problem of SED reconstruction, but it is marred by several problems. Spectroscopy is usually less accurately calibrated than photometry. Spectra are also difficult to obtain for objects at the limiting magnitude of the *Euclid* survey (AB limiting magnitude for 5σ point-like sources are estimated to be 26.2 in I_E and 24.5 in Y_E , J_E , and H_E , as reported in [Euclid Collaboration: Scaramella et al. \(2022\)](#), and unfeasible for a sufficiently large number of galaxies to meet the aims of the mission.

SED reconstruction represents a challenging task since galaxy SEDs encode important information on scales significantly smaller than the width of standard broad and medium-band filters. Therefore, a limited wavelength sampling of the I_E filter, combined with photometric inaccuracies, can lower the accuracy of the reconstruction.

In the *Euclid* survey, galaxy SEDs are one of the products of the photometric-redshift processing function (PHZ PF; [Euclid Collaboration: Tucci et al. 2025](#)), a pipeline responsible for source photometric classification (into stars, galaxies, and quasars), photometric redshift estimates for the *Euclid* core science, and galaxy physical properties for legacy science.

In this paper we conduct a study on galaxy SED reconstruction and its accuracy within the PHZ PF, using broad- and medium-band photometry present in the COSMOS field ([Scoville et al. 2007](#)), which is part of the *Euclid* Auxiliary Fields (EAFs; [Euclid Collaboration: Aussel et al. \(2025\)](#); [Euclid Collaboration: McPartland et al. \(2025\)](#)). The EAFs (COSMOS, CDFS, SXDS, VVDS, AEGIS, GOODS-N) provide deep multi-wavelength data that are used to calibrate

photometric redshifts, control the systematics in cosmic shear analyses, and characterise the galaxy sample of the EWS. In the context of this work, they constitute a sufficiently dense sampling of the I_E passband to enable an accurate SED reconstruction. However, for most of the EWS area where only VIS and NISP photometry is available, the medium-band information is missing. The methodology developed in this work is therefore designed for galaxies in the EAFs, using their broad- and medium- band photometry to reconstruct their SEDs. These then form the reference sample for the EWS, where the Nearest Neighbour Photometric Redshifts algorithm (NNPZ), described in [Euclid Collaboration: Tucci et al. \(2025\)](#), assigns to each galaxy a reconstructed SED obtained as the weighted mean of its 30 closest neighbours in flux space.

In our work, we first investigate the optimal sampling of the I_E filter, and we compare the different reconstruction approaches mentioned above. Our goal is to establish a robust method to be used in PHZ PF for galaxy SED reconstruction, and to assess whether it achieves an accuracy level that is high enough to pass the requirements set for the *Euclid* PSF model. Our work is therefore complementary to EH18: whereas they quantified feasibility, here we explore methodological strategies to minimise the bias in the SED, so that it does not exceed the accuracy level imposed on the PSF.

As indicated in C13, the size and ellipticity of the chromatic PSF change with the SED of the source and the filter transmission as a function of wavelength. The corresponding error budget, defined as the uncertainty in the PSF model due to the wavelength dependence of the PSF (and therefore directly propagating from the inaccuracies on the SEDs) is estimated to be $b = 3.5 \times 10^{-4}$. In the framework of this mission, an SED estimation that does not lead to PSF errors exceeding such a bias prevents a scenario in which dominant systematic effects are introduced in the PSF model, subsequently affecting cosmological inferences.

Working with simulated galaxy SEDs, we start our analysis studying the impact that the scheme adopted to sample the I_E filter (defined according to how homogeneous and dense is the coverage of the passband) has on the SED reconstruction. Then we present a description of the metric we use to assess the accuracy of the SED reconstruction, followed by a detailed overview of GP and TF methods. We proceed by showing the results of the SED reconstruction through the available medium and broad-band photometry, comparing the different methodologies, and we discuss a combination of the approaches that minimises the bias in the SED metric. The SED reconstruction studied in this work is implemented in the *Euclid* PHZ PF.

Finally, we present a new set of medium-band (MB) filters for the Subaru telescope, which ensures an evenly-spaced coverage of the I_E window, and we show that with this optimization it is possible to use a variety of reconstruction methods always meeting the *Euclid* requirements.

In this analysis, we adopt the *Planck* 2018 cosmology ([Planck Collaboration et al. 2020](#)): $H_0 = 67.4 \text{ km s}^{-1} \text{ Mpc}^{-1}$, $\Omega_m = 0.315$, and $\Omega_\Lambda = 0.685$.

2. The SED metric

In this section we assess how the sampling scheme of the I_E filter affects the accuracy we can achieve in the SED reconstruction. We calculate the fluxes at the sampled wavelengths by integrating the SEDs over idealised top-hat filters, and we interpolate the flux points to reconstruct the galaxy SEDs. We repeat this process at different sampling frequencies and assess the variations

in accuracy. The latter is quantified through a metric that is able to translate the uncertainty on the SED reconstruction into bias in the PSF model.

2.1. The *Euclid* PSF model and the SED metric

The *Euclid* PSF model describes the PSF of a galaxy given its position, SED and telescope properties. As reported in [Euclid Collaboration: Mellier et al. \(2025\)](#), it has been implemented as part of the *Euclid* PSF toolkit which will be fully presented in a future publication (Duncan et al., in prep.).

In the *Euclid* PSF model, the PSF of a galaxy, $\mathbf{P}_{\text{gal}}(\mathbf{p})$, at position $\mathbf{p} = (x_{\text{fov}}, y_{\text{fov}})$ in the field of view, is computed as

$$\mathbf{P}_{\text{gal}}(\mathbf{p}) = \mathcal{O} \left[\frac{\int d\lambda T(\lambda, \mathbf{p}) \lambda S_{\text{gal}}(\lambda) \mathbf{P}(\lambda, \mathbf{p})}{\int d\lambda T(\lambda, \mathbf{p}) \lambda S_{\text{gal}}(\lambda)} \right], \quad (1)$$

where $T(\lambda, \mathbf{p})$ is the throughput of the telescope and the I_E instrument at position \mathbf{p} , $\lambda S_{\text{gal}}(\lambda)$ denotes the galaxy SED expressed in photon counts per unit wavelength (up to a constant $1/hc$), and $\mathbf{P}(\lambda, \mathbf{p})$ is the monochromatic PSF at that position in the field of view. The operation \mathcal{O} accounts for non-linear instrumental effects, such as the brighter-fatter effect and charge transfer inefficiencies. These effects, studied in [Massey et al. \(2014\)](#) and [Israel et al. \(2015\)](#), are currently not included in the *Euclid* PSF model and fall out of the scope of this work.

In Eq. (1), the wavelength dependence of the PSF clearly illustrates the link between the galaxy SED and the PSF model. Furthermore, the role of the *Euclid* PSF model is to provide values for T and \mathbf{P} , so that a PSF can be created for any given SED at any position in the field of view. The model numerically evaluates Eq. (1) integrating over a set of monochromatic PSFs. Indeed, our goal here is purely to reconstruct galaxy SEDs to limit the bias into the PSF. The resolution adopted for estimating the galaxy SED is discussed in Sect. 2.2.

For *Euclid*, requirements on the PSF model are defined in terms of the PSF size and ellipticity metrics. These are characterised using quadrupole moments, which are second-order statistical measures of the PSF light distribution. The complex distortion effects influencing the size and shape of the PSF cause light to spread out far from the central peak so that, when integrating the light distribution of the PSF, the moments continue to increase or do not settle to a stable value. A standard solution to this problem is to apply a Gaussian weight function, W_{xy} , which emphasises the central peak of the PSF and attenuates the outer regions. Assuming that the centroid of the PSF is at the centre of the image (x_0, y_0) , we calculate the quadrupole moments as

$$Q_{11} = \frac{\sum_{xy} P_{xy} W_{xy} (x - x_0)^2}{\sum_{xy} P_{xy} W_{xy}}, \quad (2)$$

$$Q_{12} = \frac{\sum_{xy} P_{xy} W_{xy} (x - x_0)(y - y_0)}{\sum_{xy} P_{xy} W_{xy}}, \quad (3)$$

$$Q_{22} = \frac{\sum_{xy} P_{xy} W_{xy} (y - y_0)^2}{\sum_{xy} P_{xy} W_{xy}}. \quad (4)$$

They are used to infer the PSF size (R_{PSF}^2) and ellipticity (with components ϵ_1 and ϵ_2) as

$$R^2 = Q_{11} + Q_{22}, \quad \epsilon_1 = \frac{Q_{11} - Q_{22}}{R^2}, \quad \epsilon_2 = \frac{2Q_{12}}{R^2}. \quad (5)$$

Quadrupole moments show a linear response to the PSF intensity. This implies that, when summing together multiple PSFs

as in Eq. (1), the moments get averaged and we can re-write the equations as

$$Q_{ij}(\mathbf{p}) = \frac{\int d\lambda T(\lambda, \mathbf{p}) w(\lambda, \mathbf{p}) \lambda S_{\text{gal}}(\lambda) Q_{ij}(\lambda, \mathbf{p})}{\int d\lambda T(\lambda, \mathbf{p}) w(\lambda, \mathbf{p}) \lambda S_{\text{gal}}(\lambda)} . \quad (6)$$

In Eq. (6), $Q_{ij}(\lambda, \mathbf{p})$ are the quadrupole moments of each monochromatic PSF and $w(\lambda, \mathbf{p}) < 1$ is a correction term accounting for the flux loss derived from the application of the Gaussian weight function to the PSF light distribution. By pre-computing these monochromatic quadrupole moments, the integral above can be evaluated for various choices of SED, $S_{\text{gal}}(\lambda)$.

Using the same formalism as in Eq. (1), we define the SED metric as

$$\mathcal{M}_\lambda = \frac{\int \lambda^2 T(\lambda) S_{\text{gal}}(\lambda) d\lambda}{\int \lambda T(\lambda) S_{\text{gal}}(\lambda) d\lambda} , \quad (7)$$

where $T(\lambda)$ is the I_E transmission curve. This new metric can be interpreted as the effective central wavelength of the I_E pass-band for a given SED. Thanks to its integral form encoding the information used to build the *Euclid* PSF, biases in this metric translate straightforwardly into biases in the PSF quadrupole moments, and hence into the PSF size and ellipticity. In the end, the comparison of this metric calculated using simulated and reconstructed SEDs will allow us to test the accuracy in the SED reconstruction against the *Euclid* PSF requirements.

2.2. Sampling the VIS passband

We consider a set of 10 000 simulated galaxy SEDs (simulations are described in Sect. 3). The photometric dataset of each object is computed as a set of evenly spaced wavelengths by integrating the SED over juxtaposed and adjacent idealised top-hat filters. An interpolation of the flux points reconstructs the SED of the galaxy. This process is repeated across different sets of equidistant wavelengths, each time reducing the distance between flux points ($\Delta\lambda$ hereafter), allowing us to assess the variations in accuracy on the SED reconstruction. The accuracy estimates are obtained through comparison between the simulated (true) SED and the reconstructed one.

Using Eq. (7) we compute the metric for both the simulated and the reconstructed SEDs, denoted by $\mathcal{M}_\lambda^{\text{true}}$ and $\mathcal{M}_\lambda^{\text{rec}}$. The bias is defined as the fractional error between them:

$$b = \frac{\mathcal{M}_\lambda^{\text{true}} - \mathcal{M}_\lambda^{\text{rec}}}{\mathcal{M}_\lambda^{\text{true}}} . \quad (8)$$

For every $\Delta\lambda$ we calculate the bias in the SED metric for each galaxy, obtaining an overall bias distribution, and we estimate the sampling accuracy through its median value. We assume a bias of $b = 3.5 \times 10^{-4}$ as our target accuracy. This threshold is indicated in C13 as the budget error on shear measurements in the framework of the *Euclid* mission, due to the wavelength-dependency of the PSF model. Our findings are reported in Fig. 1. The displayed trends meet the requirement on the *Euclid* PSF at $\Delta\lambda < 10$ nm and downwards, and show a progressive degradation from a binning of about 30 nm and upwards. The increasing scatter observed for $\Delta\lambda > 30$ nm arises from undersampling, failing to capture essential features of the SEDs, including emission lines, breaks, and spectral slopes, whose inclusion is critical in order to minimise errors in the reconstruction.

Our findings suggest that we should infer the galaxy SED at 55 wavelengths evenly spaced every 10 nm between 450 and

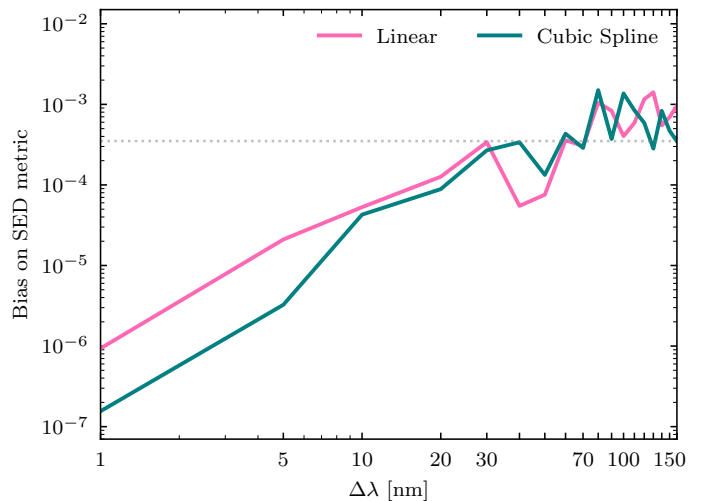


Fig. 1. Median fractional bias in the SED metric arising from the interpolation of galaxy SEDs from coarse sampling down to 1 nm sampling using linear (pink line) and cubic spline (dark green) interpolation. The dotted line represents the *Euclid* requirement set on the PSF model.

1000 nm. These results are obtained from an idealised test, where the galaxy SEDs are sampled through top-hat filters that provide a uniform and complete coverage of the I_E pass-band. When using real filter configurations (described in Sect. 3), which are non-uniformly distributed and present gaps between the filters, a larger bias is expected. From Fig. 1 we see that a sampling of $\Delta\lambda < 10$ nm is needed to ensure that the bias remains smaller than $b = 3.5 \times 10^{-4}$ when using a simple interpolation method.

3. Data

The results we present in this paper are based on measurements computed from simulated galaxy SEDs. In order for the conclusions drawn from our work to be applicable to actual *Euclid* analyses, we must ensure that these simulated data are sufficiently representative of the target galaxy population used for weak lensing cosmology. Among the *Euclid* Photometric Redshift Auxiliary fields (PHZ AUX; see [Euclid Collaboration: Mellier et al. 2025](#)), the most suitable field that can be used to build a training reference sample for galaxy SED estimation is the COSMOS field. We therefore build our simulations to represent the wide range of photometric data available in this field.

Generation of our simulated galaxy SEDs comprises two steps: construction of a galaxy population model, and then sampling from this model, including the application of an appropriate amount of photometric noise to the derived fluxes. While realism in the simulated data is important, it is not necessary that we match the galaxy population exactly.

Furthermore, we target an optimistic, best-case scenario in which we can neglect potential systematic uncertainties arising from the calibration and photometric extraction steps of the overall *Euclid* pipeline. Namely, we do not model the effects of photometric zeropoint errors, the impact of unknown wavelength variation in filter responses (see [Euclid Collaboration: Paltani et al. 2024](#)) or biases in photometric measurement due to source blending. In this way, our results will reflect the degree of accuracy that can in principle be achieved with currently-available data and the SED reconstruction methods we employ, but in practice are an upper bound to performance.

3.1. Galaxy population model

A suitable galaxy population model will consist of the evolving abundance of galaxies with redshift and luminosity, together with a description of the SEDs of those galaxies. For the former, we use pre-existing measurements of the *i*-band galaxy luminosity function produced for various tests of the *Euclid* photometric redshift pipeline, and computed using the COSMOS catalogue of [Weaver et al. \(2022\)](#). The COSMOS data were cut at $i < 25.5$ and fit with a series of single Schechter functions ([Schechter 1976](#)) in narrow redshift intervals ($\Delta z = 0.1$ at low z), widening at higher redshifts to account for the lower number density, and assuming for each galaxy that the best-fit photometric redshift given in the [Laigle et al. \(2016\)](#) catalogue is the true redshift. The standard V/V_{\max} ([Schmidt 1968](#)) estimator was used for the luminosity function and the three Schechter function parameters were then determined by the maximum a posteriori solution with flat priors in $\log_{10}(\Phi^*)$, M^* and α . Modelling the galaxy luminosity function is not the subject of this paper, and so we refer the interested reader to [Weigel et al. \(2016\)](#) for an extensive description of methods for doing so.

The second aspect of the galaxy population model is a description of the diversity of galaxy rest-frame SEDs as a function of redshift and luminosity. In recent years a number of methods have been developed with the aim of being able to rapidly produce mock galaxy samples for tasks involving simulation-based inference (e.g. [Herbel et al. 2017; Amara et al. 2021; Moser et al. 2024](#)). Typically, these methods are based upon a set of template SED components that can be linearly combined to form a total galaxy SED. An equal number of redshift-evolving Dirichlet parameters can then be fit to a known galaxy sample, which allows coefficients for these template components to be sampled when simulating a population. While these methods show great promise, they do not yet explicitly incorporate luminosity dependence in the model and so for our purposes we prefer a more direct data-driven approach. For internal consistency in our population model we use the same set of photometry that was used to measure redshifts and luminosities for the luminosity functions, namely the COSMOS catalogue of [Laigle et al. \(2016\)](#).

To build the SED model, we use the EAzY photometric redshift code ([Brammer et al. 2008](#)) to fit the set of twelve UltraVISTA ([McCracken et al. 2012](#)) SED components that are provided by the EAzY package to each galaxy, fixing their redshifts to the same ones used in the luminosity function measurement. Each catalogued object therefore has a redshift, *i*-band luminosity, and a set of template coefficients that we use to construct its rest-frame SED. The SED of our population model then consists of drawing a galaxy within an appropriate range of redshift and luminosity, and using the set of coefficients for that galaxy to build the SED. The search ranges we use are ± 0.2 in redshift and ± 0.5 mag in luminosity. If no objects lie within the search criteria, then we drop the luminosity constraint and draw from the correct interval in redshift. The basis set of linearly interpolated SED templates is reproduced in [Fig. 2](#).

3.2. Simulations of galaxy SEDs

With the galaxy population model in hand we proceed to the production of our simulated data set. We draw galaxies across the set of luminosity functions using the same cosmology as was assumed during their measurement, taking care to balance the number drawn from each redshift interval appropriately. We then assign an SED to each redshift and luminosity pair as de-

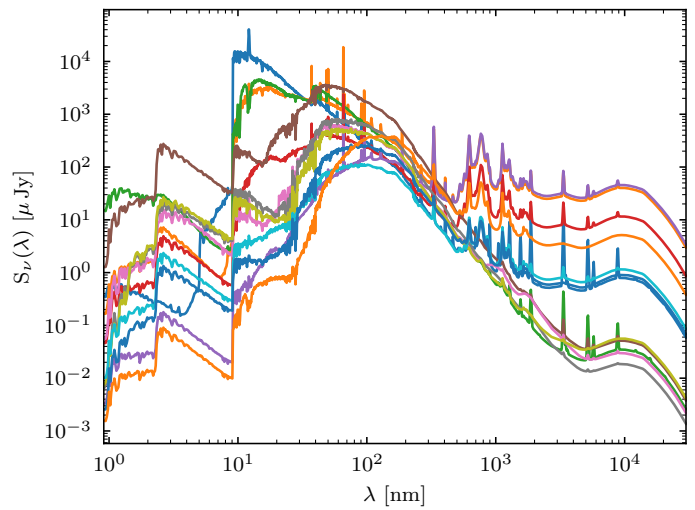


Fig. 2. Set of baseline SED templates used to build the galaxy population model, displayed in the optical to infrared window. Each galaxy is simulated through a linear combination of the elements of this basis.

scribed in the previous sub-section. We scale the amplitude of the SED such that it reflects the drawn value of *i*-band luminosity, redshift it and finally integrate it through the set of broad and medium-band passbands used in this study to obtain observed-frame noiseless fluxes.

The set of passbands we use reflects the data that are currently available in the COSMOS field, including *Euclid* observations, and are a super-set of those described in [Laigle et al. \(2016\)](#). These data will eventually be incorporated into the *Euclid* ecosystem for use within the pipeline and are taken from a range of sources in addition to *Euclid*: the DES Deep Fields (DECam *ugrizY*, [Hartley et al. 2022](#)), HSC SSP (HSC *grizy*, [Aihara et al. 2018, 2022](#)), COSMOS Suprime-Cam (SC) (*BgVriz'z''* + 12 medium bands, [Capak et al. 2007; Taniguchi et al. 2007, 2015](#)), CLAUDS (CFHT *u*, [Sawicki et al. 2019](#)), UltraVISTA (VISTA *YJHKs*, [McCracken et al. 2012](#)) and the Cosmic Dawn Survey (Spitzer IRAC ch1, ch2, [Euclid Collaboration: Moneti et al. 2022](#)). The central wavelengths, band widths, and depths (5σ , 2''-diameter apertures) of the various data sets are described in [Table 1](#). Most of these data are included in the updated COSMOS catalogue of ([Weaver et al. 2022](#)) and we adopt their measured depths. In the case of UltraVISTA, the listed depths correspond to the ultra-deep stripes as further observations have been obtained to even out the depth across the field. DECam depths for the 3-year version of the DES Deep Fields are given in [Hartley et al. \(2022\)](#) and *Euclid* depths reflect the requirements placed on the signal-to-noise ratio (S/N) of the PHZ AUX fields ([Euclid Collaboration: Mellier et al. 2025](#)).

The vast majority of galaxies that will be used in *Euclid* cosmology analyses are small on the sky, and the *Euclid* photometric pipeline produces colours through PSF-matched aperture measurements. We therefore simulate photometric noise consistently, adopting a simplified flux uncertainty model. Gaussian scatter is applied to the fluxes based on the aperture depths in [Table 1](#), with a constant aperture correction of 0.3 mag across all bands. This approach assumes perfect PSF-matching, and consequently does not capture the full S/N complexity, particularly for bright, spatially extended galaxies, where the S/N is likely to be overestimated. In this work, we do not attempt to replicate a detailed S/N-magnitude relation, as this is not expected

Table 1. Characteristics of the filters used in this work.

Filter Name	Central λ (Å)	Bandwidth (Å)	Depth
MegaCam CFHT u	3682	1200	26.50
DECam u	3876	570	25.64
SuprimeCam IA427	4263	207	24.80
SuprimeCam B	4454	892	26.50
SuprimeCam IA464	4635	218	24.30
SuprimeCam g	4771	1265	24.80
HSC g	4812	1500	26.80
DECam g	4826	1480	26.46
SuprimeCam IA484	4849	229	25.20
SuprimeCam IA505	5062	231	24.80
SuprimeCam IA527	5261	243	25.10
SuprimeCam V	5464	1900	25.50
SuprimeCam IA574	5764	273	24.50
HSC r	6230	1547	26.50
SuprimeCam IA624	6232	300	25.10
SuprimeCam r	6274	1960	25.80
DECam r	6432	1480	25.73
SuprimeCam IA679	6780	336	24.30
SuprimeCam IA709	7075	316	24.60
<i>Euclid</i> VIS I_E	7180	3900	25.80
SuprimeCam IA738	7360	324	24.80
SuprimeCam i	7667	2590	25.40
SuprimeCam IA767	7686	365	24.30
HSC i	7702	1471	26.30
DECam i	7826	1470	25.54
SuprimeCam IA827	8244	343	24.30
HSC z	8903	766	25.90
SuprimeCam z^+	9041	847	24.40
SuprimeCam z^{++}	9099	1335	25.00
DECam z	9178	1520	24.97
HSC Y	9771	1810	25.20
DECam Y	9899	1530	23.70
UltraVISTA Y	10214	923	24.70
<i>Euclid</i> NISP I_Y	10858	2630	24.25
UltraVISTA J	12535	1718	25.00
<i>Euclid</i> NISP I_J	13685	4510	24.25
UltraVISTA H	16454	2905	24.70
<i>Euclid</i> NISP I_H	17739	5670	24.25
UltraVISTA K_s	21540	3074	24.40

Notes. Central wavelengths and bandwidths are given in Å, depths are 5σ limiting magnitudes in 2''-diameter apertures.

to significantly impact our goal of exploring the upper limit performance of galaxy SED reconstruction methods. Finally, to account for the variations in depth level that are observed in most of the bands that are used for the SED reconstruction, we apply an object-by-object Gaussian scatter to the expected depths at the level of 0.1–0.3 mag, depending on the band. At constant noiseless apparent brightness, the simulated signal to noise will vary from object to object within a band. After noise is applied, we discard any galaxies for which $I_E > 25.5$, ensuring a sample that is sufficiently deep for our analysis and includes objects that could be up-scattered from fainter magnitudes in the EWS. We continue the simulation until we reach a sample of 60 000 accepted objects.

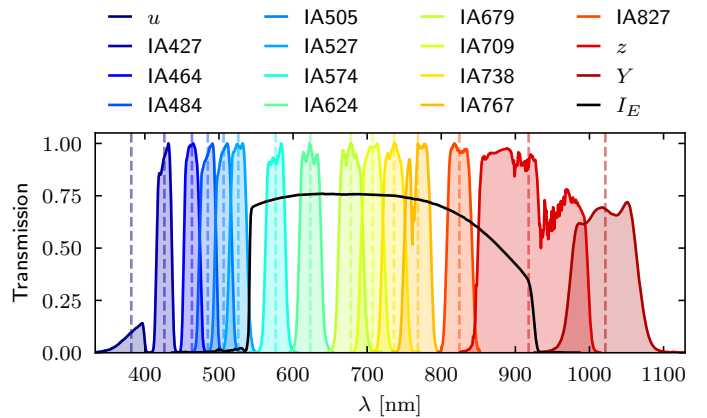


Fig. 3. Coverage of the I_E filter obtained using the Subaru SC medium band filters, and the broad pass-bands u and z from DECam and Y from VISTA VIRCam. The vertical dashed lines are placed at the weighted central wavelength of each filter.

4. Flux and SED reconstruction

In Sect. 2 we described the tests conducted to assess the sampling scheme of the I_E filter that minimises the bias in the SED metric. In order to attain this optimal scheme, we examine different techniques: (i) interpolation methods, such as linear and b-spline interpolation; (ii) GP, a machine-learning algorithm which is purely based on data; and (iii) a template-fitting based approach, which is driven by physics. We describe (ii) and (iii) in the following paragraphs, including the detailed techniques we adopt for SED reconstruction and bias estimation.

4.1. Gaussian processes

Data-driven approaches process the photometric point fluxes in order to obtain a mathematical model that we can use to predict the fluxes at all wavelengths. These algorithms do not rely on SED templates. In this work we explore the performance of GP. We use the module GaussianProcessRegressor presented in Rasmussen & Williams (2005) and available in the Python library Scikit-learn (Pedregosa et al. 2011). GP is an unsupervised algorithm consisting of a main function and a covariance function, also known as *kernel*, which quantifies the correlation between data points. The advantage of this method is that it does not assume a fixed mathematical model for regression, but it starts from a distribution of functions that is updated during the fitting process according to the observed data points and their inaccuracies. The inferred output is a function averaging over a posterior model distribution. The kernel determines the smoothness and linearity of the functions. We run initial tests with two different kernels: radial basis function (RBF) and Matérn. We found that the second provides a more accurate method for SED reconstruction, therefore we choose it for the rest of the analysis. We also investigated the impact of the kernel characteristic *length scale*, which controls the correlation between flux points at different wavelength separations and which can therefore affect the smoothness of the output function. We tested both fixed length-scale values, representative of the average separation between flux points, as well as the configuration where the algorithm adaptively optimises this parameter, and we found no significant impact on the reconstruction accuracy. For more details about the regression with GP and the properties of the two kernels, and their hyperparameters, we refer the interested reader to Sect. A. We ran GP over a set of filters including the Subaru SC

medium bands, the DECam u and z , and the VIRCAM Y broad pass-bands (Fig. 3). DECam u and the VIRCAM Y are needed to constrain the SED outside of the I_E band. In a first exploratory phase of the analysis, we tested GP using different combinations of these bands, with the purpose of studying how the algorithm behaves at the bluest and reddest ends of the SED-reconstruction interval. We found that omitting either DECam u or VIRCAM Y leads to boundary effects, as the algorithm lacks anchor points at the edges and tends to extrapolate the SED incorrectly. Including both filters mitigates these artefacts and stabilises the reconstruction within the I_E passband. DECam z is also included because it partially falls within the I_E wavelength range. We exclude the other broad-bands as they tend to smooth over the SED. The output of the GP can be evaluated at any wavelength together with uncertainties.

4.2. Template-based flux correction

TF compares the photometry of each object with a library of SEDs. The latter is a set of predefined templates, representing different types of galaxies. For TF we use the *Phosphoros* package (Paltani et al., in prep). The novelty of *Phosphoros* is to offer a fully Bayesian model that has versatile prior distributions for all parameters. *Phosphoros* has already been used in the *Euclid* photo- z challenge (Euclid Collaboration: Desprez et al. 2020), whose aim was to study the precision of different techniques for photometric redshift estimation against the requirements imposed by *Euclid* cosmic-shear analyses. *Phosphoros* has been validated and compared to a similar code, *Le Phare* (Ilbert et al. 2006; Arnouts & Ilbert 2011) in Desprez et al. (2023). *Phosphoros* assigns to each input galaxy a multivariate posterior distribution including photo- z , reddening (E_{B-V}), SED-index, and luminosity. The best model from the posterior distribution provides an estimate of the fluxes at any wavelength. While the templates are usually considered sufficient to determine photometric redshifts, their small number means that they are unable to accurately infer the true SEDs, so that the reconstructed fluxes will be significantly biased. In order to mitigate this, we introduce a template-based flux correction (TFC) method, where the estimated fluxes are corrected using their neighbouring fluxes.

In the TFC approach, for each reconstructed flux we first consider its neighbouring simulated fluxes, denoted as f_L^{true} (the flux in the preceding filter, on the left) and f_R^{true} (the flux in the following filter, on the right). The best estimates of f_L^{true} and f_R^{true} are reconstructed through *Phosphoros* and denoted as f_L^{Ph} and f_R^{Ph} , respectively. Then on each side, we assume that the ratio between the true flux and the corrected one is equal to the ratio between the corresponding fluxes reconstructed through TF. This colour-corrected flux can be written as

$$\frac{f_L^{\text{true}}}{f_L^*} = \frac{f_L^{\text{Ph}}}{f_L^{\text{Ph},\text{Ph}}}, \quad \frac{f_R^{\text{true}}}{f_R^*} = \frac{f_R^{\text{Ph}}}{f_R^{\text{Ph},\text{Ph}}}, \quad (9)$$

where $f^{\text{Ph},\text{Ph}}$ is one of the 55 fluxes inferred through TF. Also, f_L^* and f_R^* are its colour-corrected values. We derive them as

$$f_L^* = \frac{f_L^{\text{true}}}{f_L^{\text{Ph}}} f^{\text{Ph},\text{Ph}}, \quad f_R^* = \frac{f_R^{\text{true}}}{f_R^{\text{Ph}}} f^{\text{Ph},\text{Ph}}. \quad (10)$$

We further manipulate f_L^* and f_R^* to get a final estimate for the flux. In this last step we take into account the distance that separates it from its neighbours on the left (d_L) and on the right (d_R).

The weighted estimated flux is calculated as

$$f^* = \frac{d_L f_L^* + d_R f_R^*}{d_L + d_R}. \quad (11)$$

This method serves to weaken the model dependence of the results, which are obtained using an idealised discrete set of templates which tends to under-represent the variety of features we observe in real galaxy SEDs.

Table 1 describes the set of filters employed in TF. Figure 4 displays the SED of a simulated galaxy, the true fluxes and their estimates from TF, and the fluxes reconstructed with TF at the 55 chosen wavelengths. The latter get a correction in colour space.

4.3. SED reconstruction

Figure 4 shows an example of reconstructed SED for a galaxy randomly drawn from the simulated dataset. To evaluate the accuracy, we calculate the metric for both the true and the inferred galaxy SED and estimate the bias, as explained in Sect. 2. Next, we divide the galaxy sample into redshift bins, using the photometric redshift determined through TF with *Phosphoros*. We target redshifts up to $z = 3$ and set a bin width of 0.2. For each galaxy falling in a certain redshift bin, we calculate the bias in the SED metric, obtaining a bias distribution for each bin. By averaging the values in each distribution, we assess how the accuracy in SED reconstruction varies as a function of redshift. To avoid constraining the galaxy sample to specific redshift intervals, we shift the redshift bins and recompute the average SED metric using the galaxies in the new bins. The results of this analysis are presented in the next section.

5. Results

Following the methods for galaxy SED reconstruction outlined above, we study the bias in the SED metric as a function of photometric redshift. The results from TFC and GP are shown in Fig. 5. We observe that the different reconstruction methods meet the *Euclid* requirements only in certain redshift intervals, which differ between approaches. More specifically, our findings indicate that GP can ensure SED reconstruction below the bias requirement in the redshift interval [1.1, 1.8], with lower accuracy in the other ranges, where – however – TFC proves to be more robust. Figure 6 shows that linear and b-spline interpolation methods, which perform well at low redshift, do not maintain the same accuracy of TFC and GP in the remaining redshift intervals. We also quantify the dispersion of the individual bias in the SED metric in each redshift bin, finding an average value of 0.001 for TFC, 0.005 for GP, and 0.015 for the interpolation methods. Therefore, TFC and GP yield lower dispersion in the bias in the SED metric bias compared to interpolation methods, proving their robustness in the reconstruction.

The results suggest the use of a combined method for reconstructing galaxy SEDs. This approach involves both TFC and GP, applied to different photometric redshift intervals. In this way it is possible to perform SED reconstruction, using existing photometric data of the COSMOS field, with an accuracy that passes the requirements imposed by the *Euclid* mission PSF model in the majority of tomographic bins.

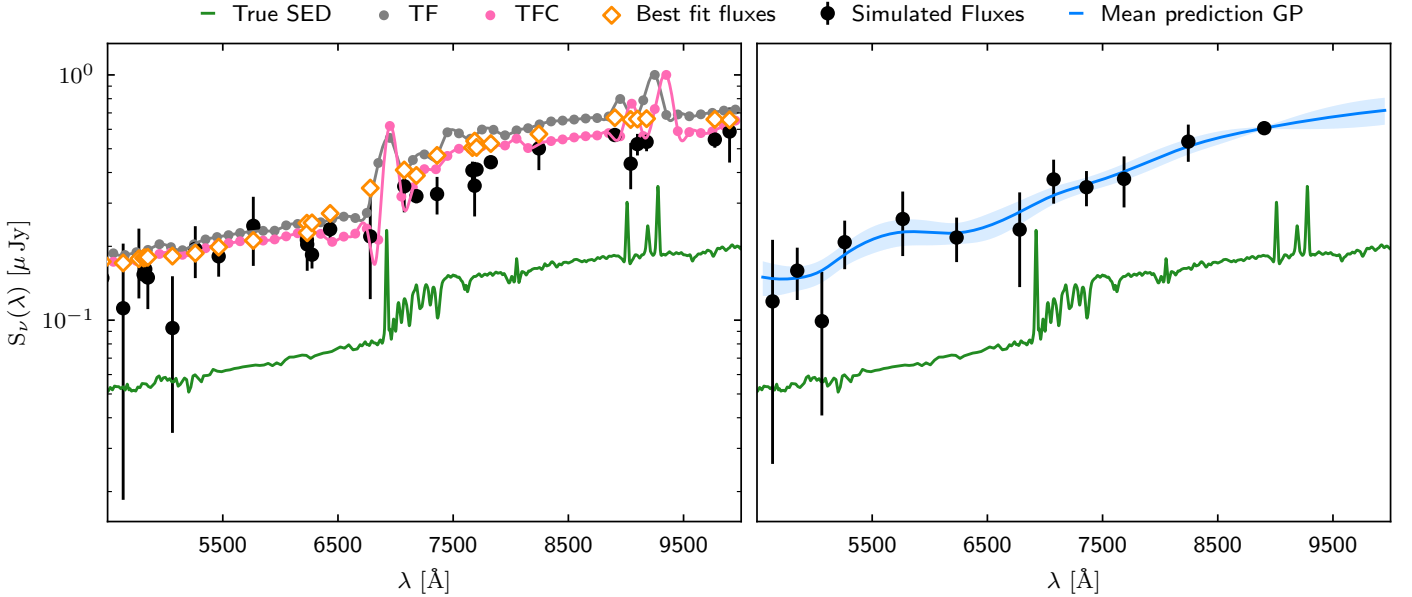


Fig. 4. Example of SED reconstruction for a galaxy randomly drawn from the simulated sample. The true SED is plotted in green. *Left panel*: example of SED reconstruction using template-based flux correction (TFC). The black points are the true fluxes known from simulations, and the orange-contoured white diamonds represent their best-fit estimates. The grey line shows the SED reconstructed with TF only, and the pink line is the colour correction. True and reconstructed SEDs are shifted in flux to enhance readability. *Right panel*: example of SED reconstruction using GP regression starting from the subset of medium-band simulated fluxes. The blue line (with the respective 95% confidence intervals) shows the inferred galaxy SED using the Matérn kernel.

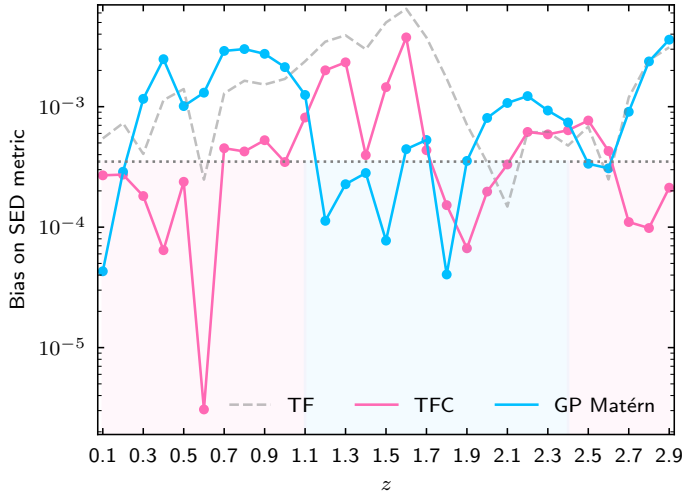


Fig. 5. Bias in SED metric as a function of photometric redshift, calculated using different methods for SED reconstruction: colour-space corrected TF (TFC; magenta) and GP (blue). The plot displays the bias averaged over single redshift bins. The dashed grey line represents the results obtained with TF before colour correction. The dotted horizontal line highlights the contribution of the PSF wavelength-dependency to the bias accounted for the *Euclid* PSF model.

6. Discussion

6.1. Performance of SED reconstruction methods

Our findings demonstrate that a careful analysis of the bias introduced in the reconstruction of galaxy SEDs can highlight the strengths of various adopted methods, allowing us to combine them and optimise the accuracy achieved in the reconstruction itself. The combination of TFC and GP is shown to be capable of meeting the requirements imposed on a mission like *Euclid*,

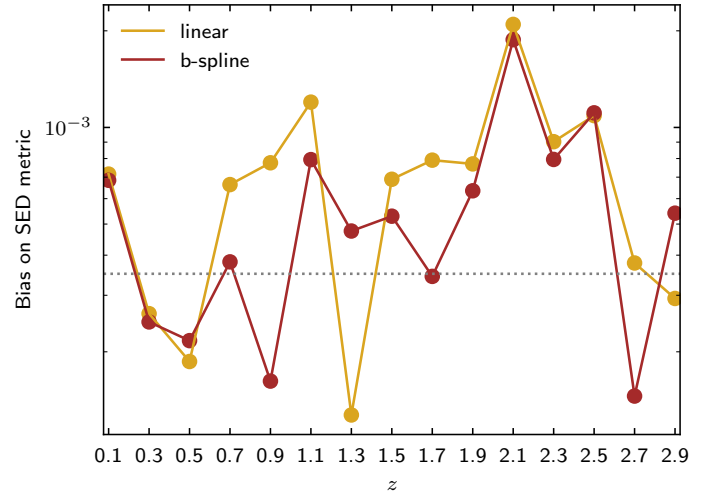


Fig. 6. Bias in the SED metric averaged over single redshift bins, calculated from the SED reconstruction using linear (sand-coloured) and b-spline (in brown) interpolation, respectively.

as defined in C13, except for a limited amount of redshift bins where the bias trend fluctuates close to the tolerance level.

GP regression is used to infer the overall galaxy SED using the available medium-band photometry. In this approach, features that are typical of galaxy SEDs are smoothed out. This is due to the nature of GP, which is purely data-driven and does not follow specific prescriptions given by the underlying physics of galaxies. More precisely, the H α emission line falls within the I_E filter up to redshift $z \approx 0.37$, H β is contained in the interval $z \in [0.13, 0.85]$, and O III in $z \in [0.10, 0.80]$. The Balmer break lies within the I_E window for $z \in [0.51, 1.47]$. The inability of GP to capture such SED sharp features can potentially introduce errors in the SED reconstruction, which explains

their poor performance up to $z \simeq 1.1$. In the redshift interval [1.1, 1.8] spectral features become broadened or are poorly sampled by the available photometry. TFC, which relies on matching the latter to a discrete set of templates through the presence of identifiable spectral features, may therefore suffer from template mismatch, leading to a degradation of the reconstruction accuracy. By contrast, GP tend to smooth the trend, resulting in a better performance where the continuum dominates or sharp features do not provide strong constraints. To summarise, TFC and GP show stability in mutually exclusive z bins and can be used to complement each other.

6.2. Galaxy SED reconstruction in the *Euclid* PHZ PF

The results presented in this work have been directly implemented in *Euclid* PHZ PF, where galaxy SEDs are part of the products delivered to enable both *Euclid* core and legacy science. The strategy adopted within the pipeline is to recover galaxy SEDs as a set of flux points evenly spaced every 10 nm in the I_E passband, corresponding to 55 narrow-band top-hat idealised filters. This choice originates from the analysis presented in Sect. 2.2, which shows that coarser sampling schemes would introduce systematic effects exceeding the constraints imposed on the *Euclid* PSF.

SEDs are reconstructed within the PHZ PF using the NNPZ algorithm, which recovers information on *Euclid* galaxies combining a reference sample with a nearest-neighbour approach (more details in [Euclid Collaboration: Tucci et al. 2025](#)). Reference samples used to infer star SEDs are built from *Gaia* BP/RP spectrophotometry matched to *Euclid* sources, assuming that *Gaia* fully covers all stellar types and metallicities across the *Euclid* footprint. Narrow-band fluxes in the 55 filters are computed by integrating the *Gaia* spectra. A similar approach is not feasible for galaxy SEDs, as spectrophotometric datasets are incomplete and fail to match *Euclid*'s depth. Therefore, reference samples are drawn from special fields like COSMOS, and galaxy SEDs are reconstructed following the methodology developed in this work, combining TFC and GP.

This implementation ensures that the PHZ PF produces galaxy SEDs within the accuracy level required for chromatic PSF in most z bins. The methodological framework established here has thus become a key component of the *Euclid* PHZ pipeline, building upon the previous feasibility studies on the *Euclid* chromatic PSF and serving an operational requirement of the mission.

6.3. Galaxy SEDs with a new set of HSC medium-band filters

As stressed above, the SED reconstruction presented so far is limited by the COSMOS dataset, which is uneven across the I_E filter, and provides only a poor coverage towards the red end of the passband. In this section we describe the results obtained running our reconstruction pipeline on galaxies simulated from a new set of filters. More precisely, we forecast the accuracy we could reach if galaxy SEDs were reconstructed starting from a newly fabricated set of 16 Subaru/Hyper Suprime-Cam (HSC) medium-band filters spaced every ~ 30 nm and evenly distributed across the I_E window¹. The MB are organised in four quadrants (MBQ1–4), with the first (MBQ1) already commis-

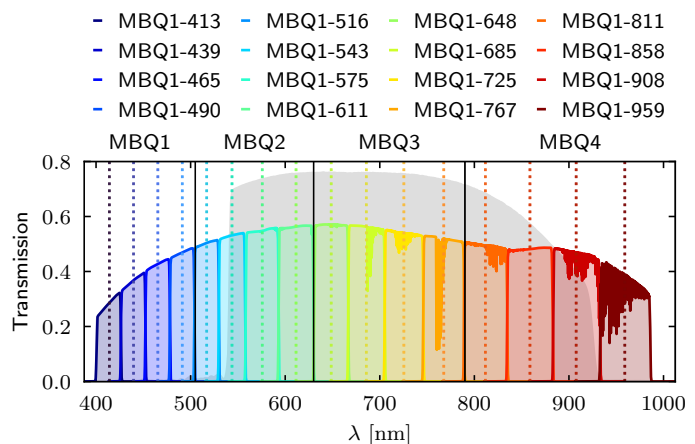


Fig. 7. The new HSC medium-band filter design, with 16 filters organised in four quadrants (MBQ1–4). Each filter is named after its weighted central wavelength, indicated by a dashed vertical line. The I_E filter is shown in the background.

sioned². This new filter design is displayed in Fig. 7. The filter transmission curves include the following effects:

- the quantum efficiency of the CCD, which is the fraction of photons that the CCD can convert into electronic signal;
- the dewar window sealing the CCD to reduce thermal noise. It can absorb or reflect a small portion of light, therefore affecting the transmission;
- the transmittance of the Primary Focus Unit of the HSC, quantifying how much light is allowed through the optics;
- the reflectivity of the primary mirror of the Subaru telescope, measuring the fraction of light reflected by the mirror at different wavelengths;
- the atmospheric absorption at Mauna Kea.

A catalogue of simulated photometry (for ~ 1 h exposure time) and synthetic spectra, based on the EL COSMOS DR1 release ([Saito et al. 2020](#)), serves as baseline for our interpolation and regression methods for SED reconstruction. Table 2 summarises the properties of each filter.

Analogously to the steps followed across the analyses presented in this paper, we calculate the bias in the SED metric for a set of 60 000 simulated galaxies, and we study its trend as a function of redshift. The results, reported in Fig. 8, show that an even sampling of the I_E filter, not exceeding the rate of ~ 30 nm, leads both TFC and GP to a more accurate and robust SED reconstruction. Similar behaviour is observed in the application of interpolation methods, as displayed in Fig. 9. In this case, the dispersion of the bias estimates per redshift bin is reduced to an average of 0.005.

6.4. Future perspectives

6.4.1. Machine-learning-based template adaptation

An alternative approach worth exploring is to model the residuals between the observed fluxes and the TF predictions using GP. In this method, GP regression is set to capture finer deviations from typical galaxy features not well represented in the templates, but still preserving the overall SED shape. This method may lead to a better reconstruction of sharp spectral features, although it remains subject to the same limitations with respect to

¹ For more details we refer the reader to <https://subarutelescope.org//Observing/Instruments/HSC/sensitivity.html>.

² Detailed information on MBQ1 can be found at https://subarutelescope.org/Instruments/HSC/fig/HSC_mbq1.png.

Table 2. Characteristics of the new HSC-MB survey with the Subaru telescope.

Filter Name	Central λ [nm]	Bandwidth [nm]	Limiting magnitude [mag]		
			$T_{\text{exp}} = 5$ min	$T_{\text{exp}} = 10$ min	$T_{\text{exp}} = 60$ min
MB413	413.34	25.87	25.04	25.43	26.41
MB439	439.20	25.87	25.14	25.52	26.51
MB465	465.10	25.82	25.09	25.47	26.45
MB490	490.98	25.87	25.33	25.71	26.69
MB516	516.86	25.87	25.57	25.95	26.93
MB543	543.63	27.66	25.26	25.64	26.62
MB575	575.64	34.72	24.91	25.28	26.26
MB611	611.40	36.78	24.66	25.04	26.02
MB648	648.62	36.04	24.71	25.09	26.07
MB685	685.92	38.53	24.64	25.02	26.00
MB725	725.58	40.76	24.70	25.08	26.06
MB767	767.53	43.13	24.17	24.55	25.52
MB811	811.92	45.61	24.16	24.54	25.58
MB858	858.67	47.85	24.02	24.40	25.43
MB908	908.24	49.66	23.74	24.12	25.15
MB959	959.54	52.91	23.38	23.75	24.79

Notes. The table includes limiting depths for different exposure times.

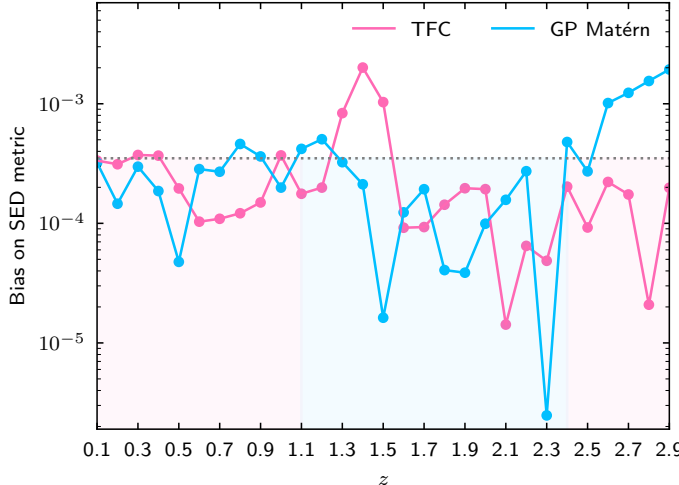


Fig. 8. Bias in the SED metric calculated on galaxy SEDs reconstructed through a photometric dataset based on the filter design proposed in Fig. 7. Magenta and brown lines display the accuracy reached through TFC and GP, respectively.

broad-band smoothing. We leave a detailed investigation of this adaptive correction strategy to future work.

6.4.2. Other sources of bias

In relation to the analysis presented in this work, we comment on three additional sources of uncertainty. First, sample variance may arise when reference samples are built from limited sky areas such as COSMOS, which may lack a complete representation of the overall galaxy population. On the other hand, as emphasised by EH18, using the same photometric data for both for photo- z and for the SED reconstruction can lead to covariance.

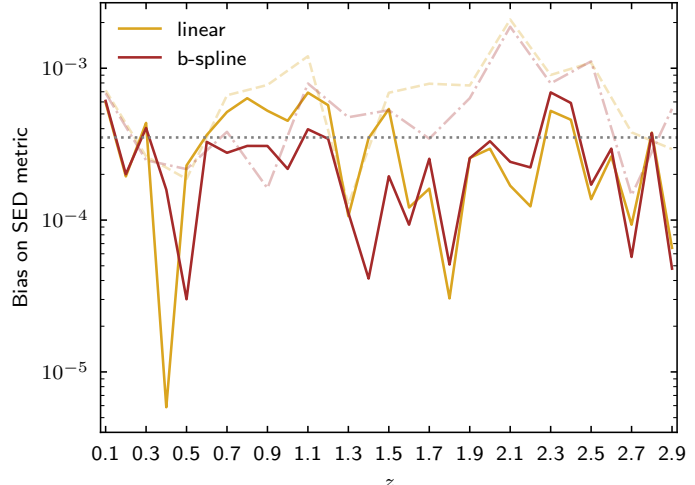


Fig. 9. Bias in the SED metric calculated using linear and b-spline interpolation, coloured in sand and brown, respectively. The bias is averaged over a distribution of uncertainties per redshift bin. Galaxy SEDs were reconstructed through a photometric dataset based on the filter design proposed in Fig. 7. For comparison, the results from Fig. 6 are also shown, with the dashed sand-coloured line representing the linear interpolation, and the dash-dotted brown line the b-spline interpolation.

The *Euclid* PHZ PF plans to mitigate the former by extending the ancillary data to the *Euclid* Auxiliary Fields (EAFs), while the latter requires a dedicated treatment of the joint inference of redshift and SEDs, which we leave for future work.

An additional source of bias is expected to arise from matching the EWS galaxies with the reference sample through NNPZ. Studying this effect is beyond the scope of the present analysis and will be assessed in a dedicated future study. The potential degradation introduced via the NNPZ step further high-

lights the importance of the new medium-band survey presented in Sect. 6.3, as it can reduce the bias already at the SED reconstruction stage.

7. Conclusions

The billions of galaxies that the *Euclid* mission will observe are set to be part of an unprecedented study of the large-scale structure of the Universe. Through the I_E broad-band filter, *Euclid* will measure their shapes with high accuracy. However, these measures strongly depend on an accurate PSF model, which is linked to the galaxy SEDs. These are reconstructed using supporting photometric datasets that provide point fluxes from available medium and broad-band filters. However, the uneven sampling of the wavelength range covered by the I_E filter can impact the reconstruction process and inaccuracies may lead to bias in the PSF model and thus in galaxy shape measurements. Studying this inaccuracy is key to minimise the bias introduced in the *Euclid* core science analyses and ensure robust constraints on cosmological parameters.

Our research focuses on the analysis of the bias in the reconstruction of galaxy SEDs for the *Euclid* mission. We introduce a novel SED metric, M_λ , interpreted as the effective central wavelength of the I_E pass-band for a given SED, and defined through the same formalism that describes the PSF quadrupole moments, quantifying the PSF size and ellipticity metrics. This ensures a direct translation of the bias in the SED metric into biases in the PSF model. According to C13, the requirement on the fractional bias in the *Euclid* PSF size metric due to wavelength dependency should remain below 3.5×10^{-4} , in order to avoid the risk of systematics on the PSF affecting cosmic shear analyses.

In this work, we explore different SED reconstruction methods, including TFC and GP, and evaluate if their performance meets the requirements imposed on the *Euclid* PSF model. Our results reveal that GP can provide accurate SED reconstruction in specific redshift intervals, while TFC exhibits robustness in other ranges, where the typical features of galaxy SEDs fall within the I_E window. Combining the strengths of both methods, we propose a combined approach that meets the *Euclid* requirements across almost all redshift bins. This methodological framework is adopted in the PHZ PF to reconstruct galaxy SEDs for the *Euclid* survey.

Furthermore, we exploit the possibility of using a newly developed filter design to improve SED reconstruction in future analyses. This new set of HSC-MB filters consists of 16 evenly spaced imaging filters which provides a quasi-spectroscopic uniform sampling of the I_E wavelength range. SED reconstruction applied on simulations based on this design demonstrates promising results, achieving an accuracy level that fulfils the *Euclid* requirements across all redshift bins.

In summary, our findings display the potential of combining physics- and data-driven approaches, offering a comprehensive strategy for achieving galaxy SED reconstruction that is close to fully meeting the requirements for the *Euclid* science mission. Notably, our results highlight that a well-designed set of evenly spaced HSC-MB filters can lead to overcome the current limitations in the SED sampling, and improve the accuracy and robustness of the SED reconstruction across all redshifts. This new infrastructure would benefit the *Euclid* core science, paving the way for future precision weak-lensing analyses.

Acknowledgements. The Euclid Consortium acknowledges the European Space Agency and a number of agencies and institutes that have supported the development of *Euclid*, in particular the Agenzia Spaziale Italiana, the Austrian Forschungsförderungsgesellschaft funded through BMIMI, the Belgian Science

Policy, the Canadian Euclid Consortium, the Deutsches Zentrum für Luft- und Raumfahrt, the DTU Space and the Niels Bohr Institute in Denmark, the French Centre National d'Etudes Spatiales, the Fundação para a Ciência e a Tecnologia, the Hungarian Academy of Sciences, the Ministerio de Ciencia, Innovación y Universidades, the National Aeronautics and Space Administration, the National Astronomical Observatory of Japan, the Nederlandse Onderzoekschool Voor Astronomie, the Norwegian Space Agency, the Research Council of Finland, the Romanian Space Agency, the Swiss Space Office (SSO) at the State Secretariat for Education, Research, and Innovation (SERI), and the United Kingdom Space Agency. A complete and detailed list is available on the *Euclid* web site (www.euclid-ec.org/consortium/community/).

References

Abbott, T. M. C., Aguena, M., Alarcon, A., et al. 2023, Phys. Rev. D, 107, 083504

Abdalla, E., Abellán, G. F., Aboubrahim, A., et al. 2022, JHEAp, 34, 49

Aihara, H., AlSayyad, Y., Ando, M., et al. 2022, PASJ, 74, 247

Aihara, H., Arimoto, N., Armstrong, R., et al. 2018, PASJ, 70, S4

Amara, A., de la Bella, L., Birrer, S., et al. 2021, JOSS, 6, 3056

Amon, A., Gruen, D., Troxel, M. A., et al. 2022, Phys. Rev. D, 105, 023514

Arnouts, S. & Ilbert, O. 2011, LePHARE, ASCL:1108.009

Asgari, M., Lin, C.-A., Joachimi, B., et al. 2021, A&A, 645, A104

Bacon, D. J. 2001, in *Cosmological Physics with Gravitational Lensing*, ed. J. Tran Thanh Van, Y. Mellier, & M. Moniez, 173

Bacon, D. J., Refregier, A. R., & Ellis, R. S. 2000, MNRAS, 318, 625

Bamba, K., Capozziello, S., Nojiri, S., & Odintsov, S. D. 2012, Ap&SS, 342, 155

Bartelmann, M. & Maturi, M. 2017, Scholarpedia, 12, 32440

Bartelmann, M. & Schneider, P. 2001, Phys. Rep., 340, 291

Brammer, G. B., van Dokkum, P. G., & Coppi, P. 2008, ApJ, 686, 1503

Capak, P., Aussel, H., Ajiki, M., et al. 2007, ApJS, 172, 99

Clifton, T., Ferreira, P. G., Padilla, A., & Skordis, C. 2012, Phys. Rep., 513, 1

Copeland, E. J., Sami, M., & Tsujikawa, S. 2006, IJMPD, 15, 1753

Cropper, M., Hoekstra, H., Kitching, T., et al. 2013, MNRAS, 431, 3103

Cypriano, E. S., Amara, A., Voigt, L. M., et al. 2010, MNRAS, 405, 494

de Jong, J. T. A., Kuijken, K., Applegate, D., et al. 2013, The Messenger, 154, 44

Desprez, G., Picouet, V., Moutard, T., et al. 2023, A&A, 670, A82

Efstathiou, G. 2025, Phil. Trans. R. Soc. A, 383, 20240022

Eriksen, M. & Hoekstra, H. 2018, MNRAS, 477, 3433

Euclid Collaboration: Aussel, H., Tereno, I., Schirmer, M., et al. 2025, A&A, submitted (Euclid Q1 SI), arXiv:2503.15302

Euclid Collaboration: Cropper, M., Al-Bahlawan, A., Amiaux, J., et al. 2025, A&A, 697, A2

Euclid Collaboration: Desprez, G., Paltani, S., Coupon, J., et al. 2020, A&A, 644, A31

Euclid Collaboration: Jahnke, K., Gillard, W., Schirmer, M., et al. 2025, A&A, 697, A3

Euclid Collaboration: McPartland, C. J. R., Zalesky, L., Weaver, J. R., et al. 2025, A&A, 695, A259

Euclid Collaboration: Mellier, Y., Abdurro'uf, Acevedo Barroso, J., et al. 2025, A&A, 697, A1

Euclid Collaboration: Moneti, A., McCracken, H. J., Shuntov, M., et al. 2022, A&A, 658, A126

Euclid Collaboration: Paltani, S., Coupon, J., Hartley, W. G., et al. 2024, A&A, 681, A66

Euclid Collaboration: Scaramella, R., Amiaux, J., Mellier, Y., et al. 2022, A&A, 662, A112

Euclid Collaboration: Schirmer, M., Jahnke, K., Seidel, G., et al. 2022, A&A, 662, A92

Euclid Collaboration: Tucci, M., Paltani, S., Hartley, W. G., et al. 2025, A&A, in press (Euclid Q1 SI), <https://doi.org/10.1051/0004-6361/202554588>, arXiv:2503.15306

Frieman, J. A., Turner, M. S., & Huterer, D. 2008, ARA&A, 46, 385

Hartley, W. G., Choi, A., Amon, A., et al. 2022, MNRAS, 509, 3547

Heisenberg, L., Kase, R., & Tsujikawa, S. 2018, Phys. Rev. D, 98, 024038

Heisenberg, L., Villarrubia-Rojo, H., & Zosso, J. 2023, Physics of the Dark Universe, 39, 101163

Herbel, J., Kacprzak, T., Amara, A., et al. 2017, J. Cosmology Astropart. Phys., 2017, 035

Heymans, C., Grocott, E., Heavens, A., et al. 2013, MNRAS, 432, 2433

Heymans, C., Van Waerbeke, L., Miller, L., et al. 2012, MNRAS, 427, 146

Hildebrandt, H., Viola, M., Heymans, C., et al. 2017, MNRAS, 465, 1454

Hoekstra, H. & Jain, B. 2008, Nucl. Phys. Rev., 58, 99

Ilbert, O., Arnouts, S., McCracken, H. J., et al. 2006, A&A, 457, 841

Israel, H., Massey, R., Prod'homme, T., et al. 2015, MNRAS, 453, 561

Kaiser, N., Wilson, G., & Luppino, G. A. 2000, arXiv e-prints, arXiv:astro-ph/0003338

Kilbinger, M. 2015, ROPP, 78, 086901

Laigle, C., McCracken, H. J., Ilbert, O., et al. 2016, ApJS, 224, 24

Laureijs, R., Amiaux, J., Arduini, S., et al. 2011, ESA/SRE(2011)12, arXiv:1110.3193

Mandelbaum, R., Hirata, C. M., Seljak, U., et al. 2005, MNRAS, 361, 1287

Massey, R., Heymans, C., Bergé, J., et al. 2007, MNRAS, 376, 13

Massey, R., Hoekstra, H., Kitching, T., et al. 2013, MNRAS, 429, 661

Massey, R., Schrabback, T., Cordes, O., et al. 2014, MNRAS, 439, 887

McCracken, H. J., Milvang-Jensen, B., Dunlop, J., et al. 2012, A&A, 544, A156

Meyers, J. E. & Burchat, P. R. 2015, ApJ, 807, 182

Monet, D. & et al. 1998, VizieR Online Data Catalog: A catalogue of astrometric standards., CDS/ADC Collection of Electronic Catalogues, 1252, 0 (1998)

Moser, B., Kacprzak, T., Fischbacher, S., et al. 2024, J. Cosmology Astropart. Phys., 2024, 049

Nojiri, S., Odintsov, S. D., & Oikonomou, V. K. 2017, Phys. Rep., 692, 1

Paulin-Henriksson, S., Amara, A., Voigt, L., Refregier, A., & Bridle, S. L. 2008, A&A, 484, 67

Pedregosa, F., Varoquaux, G., Gramfort, A., et al. 2011, Journal of Machine Learning Research, 12, 2825

Perivolaropoulos, L. & Skara, F. 2022, New A Rev., 95, 101659

Perlmutter, S., Aldering, G., Goldhaber, G., et al. 1999, ApJ, 517, 565

Planck Collaboration, Aghanim, N., Akrami, Y., et al. 2020, A&A, 641, A6

Racca, G. D., Laureijs, R., Stagnaro, L., et al. 2016, in Society of Photo-Optical Instrumentation Engineers (SPIE) Conference Series, Vol. 9904, Space Telescopes and Instrumentation 2016: Optical, Infrared, and Millimeter Wave, ed. H. A. MacEwen, G. G. Fazio, M. Lystrup, N. Batalha, N. Siegler, & E. C. Tong, 99040O

Rasmussen, C. E. & Williams, C. K. I. 2005, Gaussian Processes for Machine Learning (The MIT Press)

Riess, A. G., Filippenko, A. V., Challis, P., et al. 1998, AJ, 116, 1009

Saito, S., de la Torre, S., Ilbert, O., et al. 2020, MNRAS, 494, 199

Sawicki, M., Arnouts, S., Huang, J., et al. 2019, MNRAS, 489, 5202

Schechter, P. 1976, ApJ, 203, 297

Schmidt, M. 1968, ApJ, 151, 393

Scoville, N., Aussel, H., Brusa, M., et al. 2007, ApJS, 172, 1

Secco, L. F., Samuroff, S., Krause, E., et al. 2022, Phys. Rev. D, 105, 023515

Semboloni, E., Hoekstra, H., Huang, Z., et al. 2013, MNRAS, 432, 2385

Stölzner, B., Wright, A. H., Asgari, M., et al. 2025, arXiv e-prints, arXiv:2503.19442

Taniguchi, Y., Kajisawa, M., Kobayashi, M. A. R., et al. 2015, PASJ, 67, 104

Taniguchi, Y., Scoville, N., Murayama, T., et al. 2007, ApJS, 172, 9

Troxel, M. A., MacCrann, N., Zuntz, J., et al. 2018, Phys. Rev. D, 98, 043528

Turner, M. S. 2022, Nucl. Phys. Rev., 72, 1

Van Waerbeke, L., Mellier, Y., Radovich, M., et al. 2001, A&A, 374, 757

Weaver, J. R., Kauffmann, O. B., Ilbert, O., et al. 2022, ApJS, 258, 11

Weigel, A. K., Schawinski, K., & Bruderer, C. 2016, MNRAS, 459, 2150

Weinberg, D. H., Mortonson, M. J., Eisenstein, D. J., et al. 2013, Phys. Rep., 530, 87

Wittman, D. M., Tyson, J. A., Bernstein, G. M., et al. 1998, in Society of Photo-Optical Instrumentation Engineers (SPIE) Conference Series, Vol. 3355, Optical Astronomical Instrumentation, ed. S. D'Odorico, 626–634

Wittman, D. M., Tyson, J. A., Kirkman, D., Dell'Antonio, I., & Bernstein, G. 2000, Nature, 405, 143

Wright, A. H., Stölzner, B., Asgari, M., et al. 2025, A&A, 703, A158

Authors and affiliations

Euclid Collaboration: F. Tarsitano^{*1,2}, C. Schreiber³, H. Miyatake^{4,5,6}, A. J. Nishizawa^{7,4}, W. G. Hartley², L. Miller⁸, C. Cragg^{8,9}, B. Csizi¹⁰, H. Hildebrandt¹¹, B. Altieri¹², A. Amara¹³, S. Andreon¹⁴, N. Auricchio¹⁵, C. Baccigalupi^{16,17,18,19}, M. Baldi^{20,15,21}, A. Balestra²², S. Bardelli¹⁵, A. Biviano^{17,16}, E. Branchini^{23,24,14}, M. Brescia^{25,26}, J. Brinchmann^{27,28,29}, S. Camera^{30,31,32}, G. Cañas-Herrera^{33,34}, V. Capobianco³², C. Carbone³⁵, V. F. Cardone^{36,37}, J. Carretero^{38,39}, S. Casas^{40,41}, F. J. Castander^{42,43}, M. Castellano³⁶, G. Castignani¹⁵, S. Cavuoti^{26,44}, K. C. Chambers⁴⁵, A. Cimatti⁴⁶, C. Colodro-Conde⁴⁷, G. Congedo⁴⁸, C. J. Conselice⁴⁹, L. Conversi^{50,12}, Y. Copin⁵¹, F. Courbin^{52,53,54}, H. M. Courtois⁵⁵, M. Cropper⁵⁶, H. Degaudenzi², G. De Lucia¹⁷, H. Dole⁵⁷, F. Dubath², C. A. J. Duncan⁴⁸, X. Dupac¹², S. Escoffier⁵⁸, M. Farina⁵⁹, R. Farinelli¹⁵, S. Farrens⁶⁰, F. Faustini^{36,61}, S. Ferriol⁵¹, F. Finelli^{15,62}, N. Fourmanoit⁵⁸, M. Frailis¹⁷, E. Franceschi¹⁵, M. Fumana³⁵, S. Galeotta¹⁷, K. George⁶³, W. Gillard⁵⁸, B. Gillis⁴⁸, C. Giocoli^{15,21}, J. Gracia-Carpio⁶⁴, A. Grazian²², F. Grupp^{64,65}, S. V. H. Haugan⁶⁶, H. Hoekstra³⁴, W. Holmes⁶⁷, F. Hormuth⁶⁸, A. Hornstrup^{69,70}, K. Jahnke⁷¹, M. Jhabvala⁷², B. Joachimi⁹, E. Keihänen⁷³, S. Kermiche⁵⁸, A. Kiessling⁶⁷, B. Kubik⁵¹, M. Kümmel⁶⁵, M. Kunz⁷⁴, H. Kurki-Suonio^{75,76}, R. Laureijs⁷⁷, A. M. C. Le Brun⁷⁸, S. Ligorri³², P. B. Lilje⁶⁶, V. Lindholm^{75,76}, I. Lloro⁷⁹, G. Mainetti⁸⁰, D. Maino^{81,35,82}, E. Maiorano¹⁵, O. Mansutti¹⁷, S. Marcin⁸³, O. Marggraf⁸⁴, M. Martinelli^{36,37}, N. Martinet⁸⁵, F. Marulli^{86,15,21}, R. J. Massey⁸⁷, E. Medinaceli¹⁵, S. Mei^{88,89}, Y. Mellier^{★90,91}, M. Meneghetti^{15,21}, E. Merlin³⁶, G. Meylan⁹², A. Mora⁹³, M. Moresco^{86,15}, L. Moscardini^{86,15,21}, R. Nakajima⁸⁴, C. Neissner^{94,39}, S.-M. Niemi³³, C. Padilla⁹⁴, F. Pasian¹⁷, J. A. Peacock⁴⁸, K. Pedersen⁹⁵, V. Pettorino³³, S. Pires⁶⁰, G. Polenta⁶¹, M. Ponchet⁹⁶, L. A. Popa⁹⁷, L. Pozzetti¹⁵, F. Raison⁶⁴, A. Renzi^{98,99}, J. Rhodes⁶⁷, G. Riccio²⁶, E. Romelli¹⁷, M. Roncarelli¹⁵, C. Rosset⁸⁸, R. Saglia^{65,64}, Z. Sakr^{100,101,102}, A. G. Sánchez⁶⁴, D. Sapone¹⁰³, B. Sartoris^{65,17}, P. Schneider⁸⁴, T. Schrabback¹⁰, M. Scodellaggio³⁵, A. Secroun⁵⁸, G. Seidel⁷¹, S. Serrano^{43,104,42}, P. Simon⁸⁴, C. Sirignano^{98,99}, G. Sirri²¹, L. Stanco⁹⁹, J. Steinwagner⁶⁴, P. Tallada-Crespi^{38,39}, A. N. Taylor⁴⁸, H. I. Teplitz¹⁰⁵, I. Tereno^{106,107}, N. Tessore⁵⁶, S. Toft^{108,109}, R. Toledo-Moreo¹¹⁰, F. Torradeflot^{39,38}, I. Tutusaus^{42,43,101}, J. Valiviita^{75,76}, T. Vassallo¹⁷, A. Veropalumbo^{14,24,23}, Y. Wang¹¹¹, J. Weller^{65,64}, G. Zamorani¹⁵, F. M. Zerbi¹⁴, I. A. Zinchenko¹¹², E. Zucca¹⁵, V. Allevato²⁶, M. Ballardini^{113,114,15}, M. Bolzonella¹⁵, E. Bozzo², C. Burigana^{115,62}, R. Cabanac¹⁰¹, A. Cappi^{116,15}, T. Castro^{17,18,16,117}, J. A. Escartin Vigo⁶⁴, L. Gabarra⁸, J. García-Bellido¹¹⁸, S. Hemmati¹¹¹, R. Maoli^{119,36}, J. Martín-Fleitas¹²⁰, M. Maturi^{100,121}, N. Mauri^{46,21}, R. B. Metcalf^{86,15}, N. Morisset², A. Pezzotta¹⁴, M. Pöntinen⁷⁵, I. Rissi^{14,24}, V. Scottez^{90,122}, M. Sereno^{15,21}, M. Tenti²¹, M. Viel^{16,17,19,18,117}, M. Wiesmann⁶⁶, Y. Akrami^{118,123}, S. Alvi¹¹³, I. T. Andika⁶⁵, G. Angora^{26,113}, S. Anselmi^{99,98,124}, M. Archidiacono^{81,82}, F. Atrio-Barandela¹²⁵, L. Bazzanini^{113,15}, D. Bertacca^{98,22,99}, M. Bethermin¹²⁶, A. Blanchard¹⁰¹, L. Blot^{127,78}, M. Bonici^{128,35}, S. Borgani^{129,16,17,18,117}, M. L. Brown⁴⁹, S. Bruton¹³⁰, A. Calabro³⁶, B. Camacho Quevedo^{16,19,17}, F. Caro³⁶, C. S. Carvalho¹⁰⁷, Y. Charles⁸⁵, F. Cogato^{86,15}, S. Conseil⁵¹, A. R. Cooray¹³¹, O. Cucciati¹⁵, S. Davini²⁴, G. Desprez⁷⁷, A. Díaz-Sánchez¹³², S. Di Domizio^{23,24}, J. M. Diego¹³³, M. Y. Elkhashab^{17,18,129,16}, A. Enia¹⁵, Y. Fang⁶⁵, A. Finoguenov⁷⁵, A. Franco^{134,135,136}, K. Ganga⁸⁸, T. Gasparetto³⁶, V. Gautard¹³⁷, E. Gaztanaga^{42,43,138}, F. Giacomini²¹, F. Gianotti¹⁵, G. Gozaliasi^{139,75}, M. Guidi^{20,15}, C. M. Gutierrez¹⁴⁰, A. Hall⁴⁸, C. Hernández-Monteagudo^{141,47}, J. Hjorth⁹⁵, J. J. E. Kajava^{142,143}, Y. Kang², V. Kansal^{144,145}, D. Karagiannis^{113,146}, K. Kiiveri⁷³, J. Kim⁸, C. C. Kirkpatrick⁷³, S. Kruk¹², M. Lattanzi¹¹⁴, L. Legrand^{147,148}, M. Lembo^{91,113,114}, F. Lepori¹⁴⁹, G. Leroy^{150,87}, G. F. Lesci^{86,15}, J. Lesgourges⁴⁰, T. I. Liaudat¹⁵¹, A. Loureiro^{152,153}, J. Macias-Perez¹⁵⁴, M. Magliocchetti⁵⁹, C. Mancini³⁵, F. Mannucci¹⁵⁵, C. J. A. P. Martins^{156,27}, L. Maurin⁵⁷, M. Miluzio^{12,157}, P. Monaco^{129,17,18,16}, A. Montoro^{42,43}, C. Moretti^{17,16,18}, G. Morgante¹⁵, S. Nadathur¹³⁸, K. Naidoo¹³⁸, P. Natoli^{113,114}, A. Navarro-Alsina⁸⁴, S. Nesseris¹¹⁸, M. Oguri^{158,159}, L. Pagano^{113,114}, D. Paoletti^{15,62}, F. Passalacqua^{98,99}, K. Paterson⁷¹, L. Patrizii²¹, A. Pisani⁵⁸, D. Potter¹⁴⁹, G. W. Pratt⁶⁰, S. Quai^{86,15}, M. Radovich²², G. Rodighiero^{98,22}, W. Roster⁶⁴, S. Sacquegna¹⁶⁰, M. Sahlén¹⁶¹, D. B. Sanders⁴⁵, E. Sarpa^{19,117,18}, A. Schneider¹⁴⁹, D. Sciotti^{36,37}, E. Sellentin^{162,34}, L. C. Smith¹⁶³, J. G. Sorce^{164,57}, K. Tanidis⁸, C. Tao⁵⁸, G. Testera²⁴, R. Teyssier¹⁶⁵, S. Tosi^{23,24,14}, A. Troja^{98,99}, M. Tucci², A. Venhola¹⁶⁶, D. Vergani¹⁵, G. Verza^{167,168}, P. Vielzeuf⁵⁸, S. Vinciguerra⁸⁵, N. A. Walton¹⁶³, and J. R. Weaver¹⁶⁹

¹ Institute for Particle Physics and Astrophysics, Dept. of Physics, ETH Zurich, Wolfgang-Pauli-Strasse 27, 8093 Zurich, Switzerland

² Department of Astronomy, University of Geneva, ch. d'Ecogia 16, 1290 Versoix, Switzerland

³ IBEX Innovations Ltd., NETPark Nexus, Thomas Wright Way, Sedgefield, TS21 3FD, UK

⁴ Kobayashi-Maskawa Institute for the Origin of Particles and the Universe, Nagoya University, Chikusa-ku, Nagoya, 464-8602, Japan

⁵ Institute for Advanced Research, Nagoya University, Chikusa-ku, Nagoya, 464-8601, Japan

⁶ Kavli Institute for the Physics and Mathematics of the Universe (WPI), University of Tokyo, Kashiwa, Chiba 277-8583, Japan

⁷ DX Center, Gifu Shotoku Gakuen University, 1-1 Takakuwanishi, Yanaizucho, Gifu, 501-6122, Japan

⁸ Department of Physics, Oxford University, Keble Road, Oxford OX1 3RH, UK
⁹ Department of Physics and Astronomy, University College London, Gower Street, London WC1E 6BT, UK
¹⁰ Universität Innsbruck, Institut für Astro- und Teilchenphysik, Technikerstr. 25/8, 6020 Innsbruck, Austria
¹¹ Ruhr University Bochum, Faculty of Physics and Astronomy, Astronomical Institute (AIRUB), German Centre for Cosmological Lensing (GCCL), 44780 Bochum, Germany
¹² ESAC/ESA, Camino Bajo del Castillo, s/n, Urb. Villafranca del Castillo, 28692 Villanueva de la Cañada, Madrid, Spain
¹³ School of Mathematics and Physics, University of Surrey, Guildford, Surrey, GU2 7XH, UK
¹⁴ INAF-Osservatorio Astronomico di Brera, Via Brera 28, 20122 Milano, Italy
¹⁵ INAF-Osservatorio di Astrofisica e Scienza dello Spazio di Bologna, Via Piero Gobetti 93/3, 40129 Bologna, Italy
¹⁶ IFPU, Institute for Fundamental Physics of the Universe, via Beirut 2, 34151 Trieste, Italy
¹⁷ INAF-Osservatorio Astronomico di Trieste, Via G. B. Tiepolo 11, 34143 Trieste, Italy
¹⁸ INFN, Sezione di Trieste, Via Valerio 2, 34127 Trieste TS, Italy
¹⁹ SISSA, International School for Advanced Studies, Via Bonomea 265, 34136 Trieste TS, Italy
²⁰ Dipartimento di Fisica e Astronomia, Università di Bologna, Via Gobetti 93/2, 40129 Bologna, Italy
²¹ INFN-Sezione di Bologna, Viale Berti Pichat 6/2, 40127 Bologna, Italy
²² INAF-Osservatorio Astronomico di Padova, Via dell'Osservatorio 5, 35122 Padova, Italy
²³ Dipartimento di Fisica, Università di Genova, Via Dodecaneso 33, 16146, Genova, Italy
²⁴ INFN-Sezione di Genova, Via Dodecaneso 33, 16146, Genova, Italy
²⁵ Department of Physics "E. Pancini", University Federico II, Via Cinthia 6, 80126, Napoli, Italy
²⁶ INAF-Osservatorio Astronomico di Capodimonte, Via Moiariello 16, 80131 Napoli, Italy
²⁷ Instituto de Astrofísica e Ciências do Espaço, Universidade do Porto, CAUP, Rua das Estrelas, PT4150-762 Porto, Portugal
²⁸ Faculdade de Ciências da Universidade do Porto, Rua do Campo de Alegre, 4150-007 Porto, Portugal
²⁹ European Southern Observatory, Karl-Schwarzschild-Str. 2, 85748 Garching, Germany
³⁰ Dipartimento di Fisica, Università degli Studi di Torino, Via P. Giuria 1, 10125 Torino, Italy
³¹ INFN-Sezione di Torino, Via P. Giuria 1, 10125 Torino, Italy
³² INAF-Osservatorio Astrofisico di Torino, Via Osservatorio 20, 10025 Pino Torinese (TO), Italy
³³ European Space Agency/ESTEC, Keplerlaan 1, 2201 AZ Noordwijk, The Netherlands
³⁴ Leiden Observatory, Leiden University, Einsteinweg 55, 2333 CC Leiden, The Netherlands
³⁵ INAF-IASF Milano, Via Alfonso Corti 12, 20133 Milano, Italy
³⁶ INAF-Osservatorio Astronomico di Roma, Via Frascati 33, 00078 Monteporzio Catone, Italy
³⁷ INFN-Sezione di Roma, Piazzale Aldo Moro, 2 - c/o Dipartimento di Fisica, Edificio G. Marconi, 00185 Roma, Italy
³⁸ Centro de Investigaciones Energéticas, Medioambientales y Tecnológicas (CIEMAT), Avenida Complutense 40, 28040 Madrid, Spain
³⁹ Port d'Informació Científica, Campus UAB, C. Albareda s/n, 08193 Bellaterra (Barcelona), Spain
⁴⁰ Institute for Theoretical Particle Physics and Cosmology (TTK), RWTH Aachen University, 52056 Aachen, Germany
⁴¹ Deutsches Zentrum für Luft- und Raumfahrt e. V. (DLR), Linder Höhe, 51147 Köln, Germany
⁴² Institute of Space Sciences (ICE, CSIC), Campus UAB, Carrer de Can Magrans, s/n, 08193 Barcelona, Spain
⁴³ Institut d'Estudis Espacials de Catalunya (IEEC), Edifici RDIT, Campus UPC, 08860 Castelldefels, Barcelona, Spain
⁴⁴ INFN section of Naples, Via Cinthia 6, 80126, Napoli, Italy
⁴⁵ Institute for Astronomy, University of Hawaii, 2680 Woodlawn Drive, Honolulu, HI 96822, USA
⁴⁶ Dipartimento di Fisica e Astronomia "Augusto Righi" - Alma Mater Studiorum Università di Bologna, Viale Berti Pichat 6/2, 40127 Bologna, Italy
⁴⁷ Instituto de Astrofísica de Canarias, E-38205 La Laguna, Tenerife, Spain
⁴⁸ Institute for Astronomy, University of Edinburgh, Royal Observatory, Blackford Hill, Edinburgh EH9 3HJ, UK
⁴⁹ Jodrell Bank Centre for Astrophysics, Department of Physics and Astronomy, University of Manchester, Oxford Road, Manchester M13 9PL, UK
⁵⁰ European Space Agency/ESRIN, Largo Galileo Galilei 1, 00044 Frascati, Roma, Italy
⁵¹ Université Claude Bernard Lyon 1, CNRS/IN2P3, IP2I Lyon, UMR 5822, Villeurbanne, F-69100, France
⁵² Institut de Ciències del Cosmos (ICCUB), Universitat de Barcelona (IEEC-UB), Martí i Franquès 1, 08028 Barcelona, Spain
⁵³ Institució Catalana de Recerca i Estudis Avançats (ICREA), Passeig de Lluís Companys 23, 08010 Barcelona, Spain
⁵⁴ Institut de Ciències de l'Espai (IEEC-CSIC), Campus UAB, Carrer de Can Magrans, s/n Cerdanyola del Vallés, 08193 Barcelona, Spain
⁵⁵ UCB Lyon 1, CNRS/IN2P3, IUF, IP2I Lyon, 4 rue Enrico Fermi, 69622 Villeurbanne, France
⁵⁶ Mullard Space Science Laboratory, University College London, Holmbury St Mary, Dorking, Surrey RH5 6NT, UK
⁵⁷ Université Paris-Saclay, CNRS, Institut d'astrophysique spatiale, 91405, Orsay, France
⁵⁸ Aix-Marseille Université, CNRS/IN2P3, CPPM, Marseille, France
⁵⁹ INAF-Istituto di Astrofisica e Planetologia Spaziali, via del Fosso del Cavaliere, 100, 00100 Roma, Italy
⁶⁰ Université Paris-Saclay, Université Paris Cité, CEA, CNRS, AIM, 91191, Gif-sur-Yvette, France
⁶¹ Space Science Data Center, Italian Space Agency, via del Politecnico snc, 00133 Roma, Italy
⁶² INFN-Bologna, Via Irnerio 46, 40126 Bologna, Italy
⁶³ University Observatory, LMU Faculty of Physics, Scheinerstr. 1, 81679 Munich, Germany
⁶⁴ Max Planck Institute for Extraterrestrial Physics, Giessenbachstr. 1, 85748 Garching, Germany
⁶⁵ Universitäts-Sternwarte München, Fakultät für Physik, Ludwig-Maximilians-Universität München, Scheinerstr. 1, 81679 München, Germany
⁶⁶ Institute of Theoretical Astrophysics, University of Oslo, P.O. Box 1029 Blindern, 0315 Oslo, Norway
⁶⁷ Jet Propulsion Laboratory, California Institute of Technology, 4800 Oak Grove Drive, Pasadena, CA, 91109, USA
⁶⁸ Felix Hormuth Engineering, Goethestr. 17, 69181 Leimen, Germany
⁶⁹ Technical University of Denmark, Elektrovej 327, 2800 Kgs. Lyngby, Denmark
⁷⁰ Cosmic Dawn Center (DAWN), Denmark
⁷¹ Max-Planck-Institut für Astronomie, Königstuhl 17, 69117 Heidelberg, Germany
⁷² NASA Goddard Space Flight Center, Greenbelt, MD 20771, USA
⁷³ Department of Physics and Helsinki Institute of Physics, Gustaf Hällströmin katu 2, University of Helsinki, 00014 Helsinki, Finland
⁷⁴ Université de Genève, Département de Physique Théorique and Centre for Astroparticle Physics, 24 quai Ernest-Ansermet, CH-1211 Genève

4, Switzerland

⁷⁵ Department of Physics, P.O. Box 64, University of Helsinki, 00014 Helsinki, Finland

⁷⁶ Helsinki Institute of Physics, Gustaf Hällströmin katu 2, University of Helsinki, 00014 Helsinki, Finland

⁷⁷ Kapteyn Astronomical Institute, University of Groningen, PO Box 800, 9700 AV Groningen, The Netherlands

⁷⁸ Laboratoire d'etude de l'Univers et des phenomenes eXtremes, Observatoire de Paris, Université PSL, Sorbonne Université, CNRS, 92190 Meudon, France

⁷⁹ SKAO, Jodrell Bank, Lower Withington, Macclesfield SK11 9FT, UK

⁸⁰ Centre de Calcul de l'IN2P3/CNRS, 21 avenue Pierre de Coubertin 69627 Villeurbanne Cedex, France

⁸¹ Dipartimento di Fisica "Aldo Pontremoli", Università degli Studi di Milano, Via Celoria 16, 20133 Milano, Italy

⁸² INFN-Sezione di Milano, Via Celoria 16, 20133 Milano, Italy

⁸³ University of Applied Sciences and Arts of Northwestern Switzerland, School of Computer Science, 5210 Windisch, Switzerland

⁸⁴ Universität Bonn, Argelander-Institut für Astronomie, Auf dem Hügel 71, 53121 Bonn, Germany

⁸⁵ Aix-Marseille Université, CNRS, CNES, LAM, Marseille, France

⁸⁶ Dipartimento di Fisica e Astronomia "Augusto Righi" - Alma Mater Studiorum Università di Bologna, via Piero Gobetti 93/2, 40129 Bologna, Italy

⁸⁷ Department of Physics, Institute for Computational Cosmology, Durham University, South Road, Durham, DH1 3LE, UK

⁸⁸ Université Paris Cité, CNRS, Astroparticule et Cosmologie, 75013 Paris, France

⁸⁹ CNRS-UCB International Research Laboratory, Centre Pierre Binétruy, IRL2007, CPB-IN2P3, Berkeley, USA

⁹⁰ Institut d' Astrophysique de Paris, 98bis Boulevard Arago, 75014, Paris, France

⁹¹ Institut d' Astrophysique de Paris, UMR 7095, CNRS, and Sorbonne Université, 98 bis boulevard Arago, 75014 Paris, France

⁹² Institute of Physics, Laboratory of Astrophysics, Ecole Polytechnique Fédérale de Lausanne (EPFL), Observatoire de Sauverny, 1290 Versoix, Switzerland

⁹³ Telespazio UK S.L. for European Space Agency (ESA), Camino bajo del Castillo, s/n, Urbanizacion Villafranca del Castillo, Villanueva de la Cañada, 28692 Madrid, Spain

⁹⁴ Institut de Física d'Altes Energies (IFAE), The Barcelona Institute of Science and Technology, Campus UAB, 08193 Bellaterra (Barcelona), Spain

⁹⁵ DARK, Niels Bohr Institute, University of Copenhagen, Jagtvej 155, 2200 Copenhagen, Denmark

⁹⁶ Centre National d'Etudes Spatiales – Centre spatial de Toulouse, 18 avenue Edouard Belin, 31401 Toulouse Cedex 9, France

⁹⁷ Institute of Space Science, Str. Atomistilor, nr. 409 Măgurele, Ilfov, 077125, Romania

⁹⁸ Dipartimento di Fisica e Astronomia "G. Galilei", Università di Padova, Via Marzolo 8, 35131 Padova, Italy

⁹⁹ INFN-Padova, Via Marzolo 8, 35131 Padova, Italy

¹⁰⁰ Institut für Theoretische Physik, University of Heidelberg, Philosophenweg 16, 69120 Heidelberg, Germany

¹⁰¹ Institut de Recherche en Astrophysique et Planétologie (IRAP), Université de Toulouse, CNRS, UPS, CNES, 14 Av. Edouard Belin, 31400 Toulouse, France

¹⁰² Université St Joseph; Faculty of Sciences, Beirut, Lebanon

¹⁰³ Departamento de Física, FCFM, Universidad de Chile, Blanco Encalada 2008, Santiago, Chile

¹⁰⁴ Satlantis, University Science Park, Sede Bld 48940, Leioa-Bilbao, Spain

¹⁰⁵ Infrared Processing and Analysis Center, California Institute of Technology, Pasadena, CA 91125, USA

¹⁰⁶ Departamento de Física, Faculdade de Ciências, Universidade de Lisboa, Edifício C8, Campo Grande, PT1749-016 Lisboa, Portugal

¹⁰⁷ Instituto de Astrofísica e Ciências do Espaço, Faculdade de Ciências, Universidade de Lisboa, Tapada da Ajuda, 1349-018 Lisboa, Portugal

¹⁰⁸ Cosmic Dawn Center (DAWN)

¹⁰⁹ Niels Bohr Institute, University of Copenhagen, Jagtvej 128, 2200 Copenhagen, Denmark

¹¹⁰ Universidad Politécnica de Cartagena, Departamento de Electrónica y Tecnología de Computadoras, Plaza del Hospital 1, 30202 Cartagena, Spain

¹¹¹ Caltech/IPAC, 1200 E. California Blvd., Pasadena, CA 91125, USA

¹¹² Astronomisches Rechen-Institut, Zentrum für Astronomie der Universität Heidelberg, Mönchhofstr. 12-14, 69120 Heidelberg, Germany

¹¹³ Dipartimento di Fisica e Scienze della Terra, Università degli Studi di Ferrara, Via Giuseppe Saragat 1, 44122 Ferrara, Italy

¹¹⁴ Istituto Nazionale di Fisica Nucleare, Sezione di Ferrara, Via Giuseppe Saragat 1, 44122 Ferrara, Italy

¹¹⁵ INAF, Istituto di Radioastronomia, Via Piero Gobetti 101, 40129 Bologna, Italy

¹¹⁶ Université Côte d'Azur, Observatoire de la Côte d'Azur, CNRS, Laboratoire Lagrange, Bd de l'Observatoire, CS 34229, 06304 Nice cedex 4, France

¹¹⁷ ICSC - Centro Nazionale di Ricerca in High Performance Computing, Big Data e Quantum Computing, Via Magnanelli 2, Bologna, Italy

¹¹⁸ Instituto de Física Teórica UAM-CSIC, Campus de Cantoblanco, 28049 Madrid, Spain

¹¹⁹ Dipartimento di Fisica, Sapienza Università di Roma, Piazzale Aldo Moro 2, 00185 Roma, Italy

¹²⁰ Aurora Technology for European Space Agency (ESA), Camino bajo del Castillo, s/n, Urbanizacion Villafranca del Castillo, Villanueva de la Cañada, 28692 Madrid, Spain

¹²¹ Zentrum für Astronomie, Universität Heidelberg, Philosophenweg 12, 69120 Heidelberg, Germany

¹²² ICL, Junia, Université Catholique de Lille, LITL, 59000 Lille, France

¹²³ CERCA/ISO, Department of Physics, Case Western Reserve University, 10900 Euclid Avenue, Cleveland, OH 44106, USA

¹²⁴ Laboratoire Univers et Théorie, Observatoire de Paris, Université PSL, Université Paris Cité, CNRS, 92190 Meudon, France

¹²⁵ Departamento de Física Fundamental, Universidad de Salamanca, Plaza de la Merced s/n, 37008 Salamanca, Spain

¹²⁶ Université de Strasbourg, CNRS, Observatoire astronomique de Strasbourg, UMR 7550, 67000 Strasbourg, France

¹²⁷ Center for Data-Driven Discovery, Kavli IPMU (WPI), UTIAS, The University of Tokyo, Kashiwa, Chiba 277-8583, Japan

¹²⁸ Waterloo Centre for Astrophysics, University of Waterloo, Waterloo, Ontario N2L 3G1, Canada

¹²⁹ Dipartimento di Fisica - Sezione di Astronomia, Università di Trieste, Via Tiepolo 11, 34131 Trieste, Italy

¹³⁰ California Institute of Technology, 1200 E California Blvd, Pasadena, CA 91125, USA

¹³¹ Department of Physics & Astronomy, University of California Irvine, Irvine CA 92697, USA

¹³² Departamento Física Aplicada, Universidad Politécnica de Cartagena, Campus Muralla del Mar, 30202 Cartagena, Murcia, Spain

¹³³ Instituto de Física de Cantabria, Edificio Juan Jordá, Avenida de los Castros, 39005 Santander, Spain

¹³⁴ INFN, Sezione di Lecce, Via per Arnesano, CP-193, 73100, Lecce, Italy

135 Department of Mathematics and Physics E. De Giorgi, University of Salento, Via per Arnesano, CP-I93, 73100, Lecce, Italy
 136 INAF-Sezione di Lecce, c/o Dipartimento Matematica e Fisica, Via per Arnesano, 73100, Lecce, Italy
 137 CEA Saclay, DFR/IRFU, Service d'Astrophysique, Bat. 709, 91191 Gif-sur-Yvette, France
 138 Institute of Cosmology and Gravitation, University of Portsmouth, Portsmouth PO1 3FX, UK
 139 Department of Computer Science, Aalto University, PO Box 15400, Espoo, FI-00 076, Finland
 140 Instituto de Astrofísica de Canarias, E-38205 La Laguna; Universidad de La Laguna, Dpto. Astrofísica, E-38206 La Laguna, Tenerife, Spain
 141 Universidad de La Laguna, Dpto. Astrofísica, E-38206 La Laguna, Tenerife, Spain
 142 Department of Physics and Astronomy, Vesilinnantie 5, University of Turku, 20014 Turku, Finland
 143 Serco for European Space Agency (ESA), Camino bajo del Castillo, s/n, Urbanizacion Villafranca del Castillo, Villanueva de la Cañada, 28692 Madrid, Spain
 144 ARC Centre of Excellence for Dark Matter Particle Physics, Melbourne, Australia
 145 Centre for Astrophysics & Supercomputing, Swinburne University of Technology, Hawthorn, Victoria 3122, Australia
 146 Department of Physics and Astronomy, University of the Western Cape, Bellville, Cape Town, 7535, South Africa
 147 DAMTP, Centre for Mathematical Sciences, Wilberforce Road, Cambridge CB3 0WA, UK
 148 Kavli Institute for Cosmology Cambridge, Madingley Road, Cambridge, CB3 0HA, UK
 149 Department of Astrophysics, University of Zurich, Winterthurerstrasse 190, 8057 Zurich, Switzerland
 150 Department of Physics, Centre for Extragalactic Astronomy, Durham University, South Road, Durham, DH1 3LE, UK
 151 IRFU, CEA, Université Paris-Saclay 91191 Gif-sur-Yvette Cedex, France
 152 Oskar Klein Centre for Cosmoparticle Physics, Department of Physics, Stockholm University, Stockholm, SE-106 91, Sweden
 153 Astrophysics Group, Blackett Laboratory, Imperial College London, London SW7 2AZ, UK
 154 Univ. Grenoble Alpes, CNRS, Grenoble INP, LPSC-IN2P3, 53, Avenue des Martyrs, 38000, Grenoble, France
 155 INAF-Osservatorio Astrofisico di Arcetri, Largo E. Fermi 5, 50125, Firenze, Italy
 156 Centro de Astrofísica da Universidade do Porto, Rua das Estrelas, 4150-762 Porto, Portugal
 157 HE Space for European Space Agency (ESA), Camino bajo del Castillo, s/n, Urbanizacion Villafranca del Castillo, Villanueva de la Cañada, 28692 Madrid, Spain
 158 Center for Frontier Science, Chiba University, 1-33 Yayoi-cho, Inage-ku, Chiba 263-8522, Japan
 159 Department of Physics, Graduate School of Science, Chiba University, 1-33 Yayoi-Cho, Inage-Ku, Chiba 263-8522, Japan
 160 INAF - Osservatorio Astronomico d'Abruzzo, Via Maggini, 64100, Teramo, Italy
 161 Theoretical astrophysics, Department of Physics and Astronomy, Uppsala University, Box 516, 751 37 Uppsala, Sweden
 162 Mathematical Institute, University of Leiden, Einsteinweg 55, 2333 CA Leiden, The Netherlands
 163 Institute of Astronomy, University of Cambridge, Madingley Road, Cambridge CB3 0HA, UK
 164 Univ. Lille, CNRS, Centrale Lille, UMR 9189 CRISTAL, 59000 Lille, France
 165 Department of Astrophysical Sciences, Peyton Hall, Princeton University, Princeton, NJ 08544, USA
 166 Space physics and astronomy research unit, University of Oulu, Pentti Kaiteran katu 1, FI-90014 Oulu, Finland
 167 Center for Computational Astrophysics, Flatiron Institute, 162 5th Avenue, 10010, New York, NY, USA
 168 International Centre for Theoretical Physics (ICTP), Strada Costiera 11, 34151 Trieste, Italy
 169 MIT Kavli Institute for Astrophysics and Space Research, Massachusetts Institute of Technology, Cambridge, MA 02139, USA

* e-mail: federica.tarsitano@phys.ethz.ch
 ** Deceased

Appendix A: Regression with Gaussian processes

GP is a machine-learning algorithm used for both classification and regression tasks. As mentioned in Sect. 4, this method does not infer a distribution over the parameters of a specific function. Instead, it is used to infer a distribution over functions. More precisely, the process works by defining a prior distribution over functions, and updating the distribution based on observed data to obtain a posterior distribution. This section describes the most salient steps covered by this process, illustrating examples recreated from the astronomical dataset used in this work. For a full treatment of the topic we refer the reader to Rasmussen & Williams (2005).

Each point in the dataset has an input value $\mathbf{x} = \{x_1, x_2, \dots, x_n\}$ corresponding to an observation $\mathbf{y} = \{y_1, y_2, \dots, y_n\}$. The goal of GP regression is to calculate a function f_* assigning an observation $y_* = f_*(x_*)$ to each new input x_* . GP associates any point \mathbf{x} to a random variable, $f(\mathbf{x})$, whose N -dimensional joint distribution, $p(f(\mathbf{x}_1), f(\mathbf{x}_2), \dots, f(\mathbf{x}_N))$, is Gaussian and defined as

$$p(\mathbf{f}|\mathbf{X}) = \mathcal{N}(\mathbf{f}|\mu, \mathbf{K}), \quad (\text{A.1})$$

where $\mathbf{f} = f(\mathbf{x}_1), f(\mathbf{x}_2), \dots, f(\mathbf{x}_N)$, $\mu = (m(\mathbf{x}_1), m(\mathbf{x}_2), \dots, m(\mathbf{x}_N))$ and $K_{ij} = \kappa(x_i, x_j)$. More precisely, μ is the sample mean function and κ is a positive definite covariance function or *kernel*. The covariance function quantifies the similarities between the points, and propagates the information into their respective observations. This means that if x_i and x_j are similar, the values of $f(x_i)$ and $f(x_j)$ are also expected to be similar. Therefore the kernel is responsible for shaping the function in terms of linearity and smoothness. The predictive distribution is given by

$$p(\mathbf{f}_*|\mathbf{X}_*, \mathbf{X}, \mathbf{f}) = \mathcal{N}(\mathbf{f}_*|\mu_*, \Sigma_*), \quad (\text{A.2})$$

where Σ_* summarises the covariance between the original input data points and the new inputs. For the latter, predictions can be made through the posterior distribution by computing the mean and variance of the distribution itself at those points. The mean provides the predicted function value, while the variance gives an estimate of the uncertainty in the prediction. In Fig. A.1 we can visualise all the concepts discussed so far. The SED of a simulated galaxy is reconstructed with GP from the set of Subaru SC medium-bands described in Sect. 4.1. First, GP builds a distribution of prior functions, $p(\mathbf{f}|\mathbf{X})$. Then the prior distribution is updated according to the function values and the correlation and the noise level of the flux points. Six functions, randomly sampled from the posterior distribution, and the mean function of the posterior distribution, f_* , are also displayed. The latter can be evaluated at any new wavelength, λ_* , falling within the λ regression range, to infer the value of the SED at that wavelength, $f_*(\lambda_*)$, with an error equal to the variance of the posterior. The GP regression is carried using a different choice of kernels, RBF in the top panel, and the Matérn kernel in the bottom panel³. The RBF kernel is given by

$$\kappa(x_i, x_j) = \exp\left(-\frac{d^2(x_i, x_j)}{2\ell^2}\right), \quad (\text{A.3})$$

where $d^2(x_i, x_j)$ is the Euclidean distance. This kernel is infinitely differentiable. This property allows the GP to have mean square derivatives of all orders. Therefore these functions are extremely smooth. The Matérn kernel is defined as

$$\kappa(x_i, x_j) = \frac{1}{\Gamma(\nu)2^{\nu-1}} \left(\frac{\sqrt{2\nu}}{\ell} d(x_i, x_j)\right)^\nu K_\nu\left(\frac{\sqrt{2\nu}}{\ell} d(x_i, x_j)\right). \quad (\text{A.4})$$

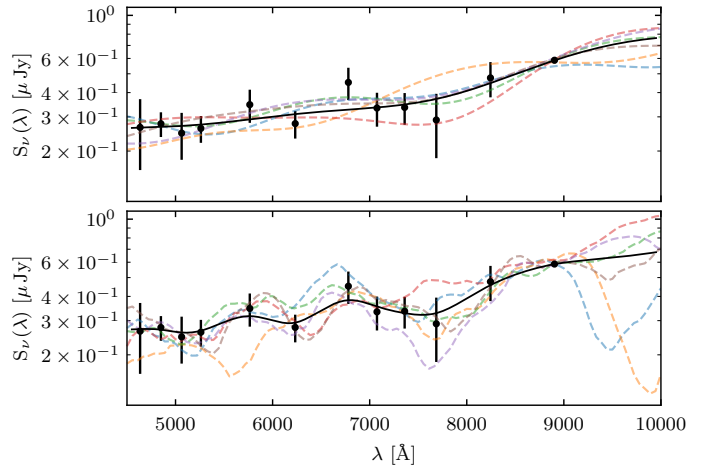


Fig. A.1. Example of SED reconstruction through GP regression for a randomly selected simulated galaxy, using the RBF kernel (top panel) and the Matérn kernel (bottom panel). The key components of the regression are illustrated, with six functions sampled from the posterior distribution (dashed coloured lines), and the mean predictive function (solid black line).

The ν parameter models the smoothness of the predictive function. It is modelled by a length-scale parameter, ℓ . This allows the kernel to recover more realistically the minute structure of the function and the similarities between the data points. As we observed in our tests and illustrated in Fig. A.1, the Matérn kernel is more suited than RBF for the task of galaxy SED reconstruction.

³ For further information we refer the reader to https://scikit-learn.org/stable/modules/gaussian_process.html.